Monthly Notices
of the
ROYAL ASTRONOMICAL SOCIETY

MNRAS **460,** 4453–4465 (2016)
Advance Access publication 2016 May 27

doi:10.1093/mnras/stw1269

Strong lensing in the inner halo of galaxy clusters

C. Saez,[1,2★] L. E. Campusano,[3] E. S. Cypriano,[4] L. Sodré[4] and J.-P. Kneib[5,6]

[1]*Korea Astronomy and Space Science Institute (KASI), 61-1, Hwaam-dong, Yuseong-gu, Deajeon 305-348, Republic of Korea*
[2]*Department of Astronomy, University of Maryland, College Park, MD 20742-2421, USA*
[3]*Observatorio Astronómico Cerro Calán, Departamento de Astronomía, Universidad de Chile, Casilla 36-D, Santiago, Chile*
[4]*Departamento de Astronomia, IAG, Universidade de São Paulo, R. do Matão 1226, Cidade Universitária, 05508-090 São Paulo, Brazil*
[5]*Laboratoire d'Astrophysique, Ecole Polytechnique Fédérale de Lausanne (EPFL), Observatoire de Sauverny, CH-1290 Versoix, Switzerland*
[6]*Aix Marseille Université, CNRS, LAM (Laboratoire d'Astrophysique de Marseille) UMR 7326, F-13388 Marseille, France*

Accepted 2016 May 25. Received 2016 April 29; in original form 2015 December 25

ABSTRACT

We present an axially symmetric formula to calculate the probability of finding gravitational arcs in galaxy clusters, being induced by their massive dark matter haloes, as a function of clusters redshifts and virial masses. The formula includes the ellipticity of the clusters dark matter potential by using a pseudo-elliptical approximation. The probabilities are calculated and compared for two dark matter halo profiles, the Navarro, Frenk and White (NFW) and the non-singular-isothermal-sphere (NSIS). We demonstrate the power of our formulation through a Kolmogorov–Smirnov (KS) test on the strong lensing statistics of an X-ray bright sample of low-redshift Abell clusters. This KS test allows us to establish limits on the values of the concentration parameter for the NFW profile (c_{Δ}) and the core radius for the NSIS profile ($r_{\rm c}$), which are related to the lowest cluster redshift ($z_{\rm cut}$) where strong arcs can be observed. For NFW dark matter profiles, we infer cluster haloes with concentrations that are consistent to those predicted by ΛCDM simulations. As for NSIS dark matter profiles, we find only upper limits for the clusters core radii and thus do not rule out a purely SIS model. For alternative mass profiles, our formulation provides constraints through $z_{\rm cut}$ on the parameters that control the concentration of mass in the inner region of the clusters haloes. We find that $z_{\rm cut}$ is expected to lie in the 0.0–0.2 redshift, highlighting the need to include very low-z clusters in samples to study the clusters mass profiles.

Key words: gravitational lensing: strong – galaxies: clusters: general – cosmology: observations – dark matter – X-rays: galaxies: clusters.

1 INTRODUCTION

Arc statistics is an important tool to test cluster structure (e.g. Wu & Hammer 1993; Bartelmann, Steinmetz & Weiss 1995; Oguri, Taruya & Suto 2001; Huterer & Ma 2004; Xu et al. 2016) and cosmology (e.g. Bartelmann et al. 1998; Li et al. 2005; Jullo et al. 2010). As a consequence, numerous arc surveys have been performed through the use of ground and space telescopes. These arc searches have been mainly based on X-ray-selected clusters (e.g. Luppino et al. 1999; Campusano et al. 2006; Merten et al. 2015), and clusters chosen in the optical (e.g. Gladders et al. 2003; Hennawi et al. 2008).

In particular, constraining the clusters dark matter halo density profile has been an objective advocated by many investigations in the last 15 years. A popular model characterizing their radial mass profile has been the Navarro, Frenk and White model (NFW; Navarro, Frenk & White 1996), also known as the 'universal profile'. The acceptance of this model is mainly due to its foundation on ΛCDM N-body simulations. The NFW is represented as $\rho(r) = \rho_{\rm s}(r/r_{\rm s})^{-1}$ $(1 + r/r_{\rm s})^{-2}$, and therefore, presents central cusps given by $\rho(r) \propto r^{-1}$. Current high-resolution ΛCDM simulations predict dark matter galaxy clusters haloes with shallow central cusps ($\mathrm{d}\log\rho/\mathrm{d}\log r \gtrsim -1.0$). However, as the radius increases, this haloes become progressively steeper and well fitted by an NFW profile (e.g. Gao et al. 2012). The baryonic mass is not considered in pure dark matter ΛCDM simulations. Its presence, could be producing steeper and more concentrated mass profiles in the central regions of the clusters (e.g. Gnedin et al. 2004). The gravitational effect of the baryonic matter has been recently studied through combined observations of strong lensing, weak lensing and resolved stellar kinematic within the brightest cluster galaxy (BCG; Newman et al. 2013a,b). These studies suggest that although the presence of baryonic dark matter near the cluster centres is significant, pure dark matter models give reliable fits to the total mass distributions. This happens even at scales where baryonic mass should be dominant.

★E-mail: csaez@kasi.re.kr

The modelling of arc and arclets also shows discrepant results regarding the mass profile describing clusters haloes. For example, Gavazzi et al. (2003) find that the cluster MS 2137 is better constrained by an isothermal profile when compared to an NFW model. On the contrary, Kneib et al. (2003) show that the mass distribution of Cl 0024+1654 strongly favours the NFW profile. Since there is still debate concerning the dark matter halo profiles of galaxy clusters (e.g. Beraldo e Silva, Lima & Sodré 2013), it is important to develop other independent methodologies to probe the haloes. Arc statistics allow the development of methodologies that are not sensitive to specific selection effects or systematic errors involved in individual observations. Besides, it is well known that the study of the lensing properties of nearby galaxy clusters ($z \lesssim 0.5$) offers an unique opportunity to investigate the cluster central regions with high spatial resolution (e.g. Campusano, Kneib & Hardy 1998; Cypriano et al. 2001).

In this paper, we present an axially symmetric formula (see e.g. Cooray 1999; Kaufmann & Straumann 2000; Cypriano et al. 2001; Oguri et al. 2001) to calculate the number of arcs produced by dark matter haloes as a function of the cluster's redshift and mass. Our formulation is also used to study departures from axial symmetry by including a pseudo-elliptical approximation (Golse & Kneib 2002) on the dark energy potential. Predictions are determined and compared for two currently competing cluster mass models, the non-singular-isothermal-sphere (NSIS) and the NFW. The goal of this work is to find parameters that could be observationally constrained through the redshift distribution of the number of arcs in a low-redshift sample of galaxy clusters.

The layout of the paper is as follows: in Section 2, we introduce the conventions used and describe our formulation to calculate the number of arcs distribution. In Sections 3.1–3.3, we analyse for NSIS and NFW profiles the parameter sensitivity of the number of arcs distribution. In Section 3.4, using our formulation, we implement a statistical test to provide constraints on parameters of the clusters dark matter haloes. This test is applied to a low-redshift X-ray bright sample of Abell clusters. In Section 4 we summarize our results. Throughout this paper, unless stated otherwise, we use cgs units, and we adopt a flat Λ-dominated universe with, $\Omega_\Lambda = 0.7$ and $\Omega_\mathrm{m} = 0.3$.

2 METHODOLOGY

2.1 Axially symmetric models in general

The dimensionless lens equation, relating the angular position of the image on the lens plane (x) with that of its source on the source plane (y) is (see e.g. Schneider, Ehlers & Falco 1992)

$$y = x - \alpha(x), \tag{1}$$

where $\alpha(x)$ is the dimensionless deflection angle, which is given by

$$\alpha(x) = \frac{2}{x}\left(\frac{4\pi G}{c^2}\frac{D_\mathrm{l}D_\mathrm{ls}}{D_\mathrm{s}}\right)\int_0^x \Sigma(\xi_0 x')x'\mathrm{d}x' = \frac{2}{x}\int_0^x \kappa(x')x'\mathrm{d}x'. \tag{2}$$

Here, $\Sigma(\xi) = \int_{-\infty}^{+\infty}\rho(\xi, z)\mathrm{d}z$ is the projected surface density, D_l, D_s and D_ls are the angular distance, to the lens, to the source and between the lens and the source. Additionally, ξ_0 is a length-scale on the lens plane and $\kappa(x) = \Sigma(\xi_0 x)/\Sigma_\mathrm{crit}$ ($\Sigma_\mathrm{crit} = c^2 D_\mathrm{s}(4\pi G D_\mathrm{l}D_\mathrm{ls})^{-1}$) is the surface mass density in units of the critical surface density for lensing. Equation (2) can also be written as $\kappa = (\alpha/x + \mathrm{d}\alpha/\mathrm{d}x)/2$.

The amplification factor of an image will be given by $\mu = |\lambda_\mathrm{t}\lambda_\mathrm{r}|^{-1}$, where λ_r and λ_t are the radial and tangential eigenvalues of the Jacobian matrix describing the image distortion in the lens equation. They are expressed as

$$\lambda_\mathrm{r} = 1 - \kappa + \gamma \quad \text{and} \quad \lambda_\mathrm{t} = 1 - \kappa - \gamma, \tag{3}$$

with $\gamma = \alpha/x - \kappa$. Under this formulation, from equations (1) and (3), $y(x) = x\lambda_\mathrm{t}(x)$. Throughout this paper, we call x_t as the value of x where $\lambda_\mathrm{t}(x_\mathrm{t}) = 0$ and x_r where $\lambda_\mathrm{r}(x_\mathrm{r}) = 0$. For tangentially elongated images $R_\mathrm{t} = \lambda_\mathrm{r}/\lambda_\mathrm{t}$ is the length-to-width ratio. The cross-section of the tangential image with length-to-width ratio greater than R_t is given by

$$\sigma_\mathrm{c}(R_\mathrm{t}) = 2\pi\int_0^{y_{R_\mathrm{t}}} y'dy' = \pi y_{R_\mathrm{t}}^2. \tag{4}$$

Notice that for $x = x_{R_\mathrm{t}}$, $\lambda_\mathrm{r}(x_{R_\mathrm{t}})/\lambda_\mathrm{t}(x_{R_\mathrm{t}}) = R_\mathrm{t}$ and $y_{R_\mathrm{t}} = x_{R_\mathrm{t}}\lambda_\mathrm{t}(x_{R_\mathrm{t}})$. Therefore, equation (4) can be written as well as

$$\sigma_\mathrm{c}(R_\mathrm{t}) = \pi\lambda_\mathrm{t}^2(x_{R_\mathrm{t}})x_{R_\mathrm{t}}^2. \tag{5}$$

The cross-section in the source coordinates is then

$$\hat{\sigma}_\mathrm{c} = \eta_0^2\sigma_\mathrm{c} = \xi_0^2\left(\frac{D_\mathrm{s}}{D_\mathrm{l}}\right)^2\sigma_\mathrm{c}, \tag{6}$$

where $\eta_0 = \xi_0 D_\mathrm{s}/D_\mathrm{l}$ is a length-scale on the source plane.

The condition $\lambda_\mathrm{r}(x_\mathrm{r}) = 0$ ($y_\mathrm{r} = |\lambda_\mathrm{r}(x_\mathrm{r})|$) will limit the region where strong lensing is possible. The brightest image in the strong lensing region is constrained to $x > x_\mathrm{t}$; $0 < y < y_\mathrm{r}$, where x_t is given from $\lambda_\mathrm{t}(x_\mathrm{t}) \equiv 0$ ($y_\mathrm{t} = 0$). The brightest radially elongated image is limited to $x_\mathrm{r} < x < x_{r_\mathrm{m}}$ and $y_{r_\mathrm{m}} < y < y_\mathrm{r}$; where $\lambda_\mathrm{t}(x_{r_\mathrm{m}})/\lambda_\mathrm{r}(x_{r_\mathrm{m}}) = -1$. The cross-section for radial images with length-to-width ratio greater than R_r is given by $\sigma_\mathrm{c}(R_r) = \pi(y_\mathrm{r}^2 - y_{R_\mathrm{r}}^2)$, where $R_\mathrm{r} = -\lambda_\mathrm{t}(x_{R_\mathrm{r}})/\lambda_\mathrm{r}(x_{R_\mathrm{r}})$ and $y_{R_\mathrm{r}} = y(x_{R_\mathrm{r}})$. Note that the condition $\mu > 1$ limits the region where strong lensing images can form. This is especially important for the formation of radial images. Throughout this paper, with exception of Appendix A, we focus our analysis of cross-sections and the statistics of arcs of the brightest images, which are the tangential. The reason is that in a survey of galaxy clusters the probability of detection of tangential images is approximately an order of magnitude greater than that of radial images (see Appendix A).

2.2 Dark matter models

In this work, we adopt two axially symmetric dark matter mass-models to describe the mass distribution of galaxy clusters: the NFW profile, and the NSIS. Here we briefly describe the strong lensing physical parameters corresponding to these models.

2.2.1 *NFW model*

The NFW radial and projected mass–density profiles are given by

$$\rho(r) = \frac{\rho_\mathrm{s}}{(r/r_\mathrm{s})(1 + r/r_\mathrm{s})^2}$$

$$\Sigma(r_\mathrm{s}\,x) = \frac{2\rho_\mathrm{s}r_\mathrm{s}}{1 - x^2}\left(\frac{1}{\sqrt{1 - x^2}}\operatorname{arctanh}\sqrt{1 - x^2} - 1\right). \tag{7}$$

For this profile, taking $\xi_0 = r_\mathrm{s}$ and defining $\kappa_\mathrm{s} = \rho_\mathrm{s}r_\mathrm{s}\Sigma_\mathrm{crit}^{-1}$ (Σ_crit defined in Section 2.1), we have that

$$\kappa(x) = \frac{2\kappa_\mathrm{s}}{1 - x^2}\left(\frac{1}{\sqrt{1 - x^2}}\operatorname{arctanh}\sqrt{1 - x^2} - 1\right) = \frac{2\kappa_\mathrm{s}}{x}\frac{\mathrm{d}g}{\mathrm{d}x}.$$

Consequently, the values of the deflection angle, γ and eigenvalues are

$$\alpha(x) = \frac{4\kappa_s}{x}\left(\ln\frac{x}{2} + \frac{1}{\sqrt{1-x^2}}\operatorname{arctanh}\sqrt{1-x^2}\right) \equiv \frac{4\kappa_s}{x}g,$$

$$\gamma(x) = \frac{2\kappa_s}{x}\left(\frac{2g}{x} - \frac{\mathrm{d}g}{\mathrm{d}x}\right),$$

$$\lambda_r(x) = 1 - \frac{4\kappa_s}{x}\left(\frac{\mathrm{d}g}{\mathrm{d}x} - \frac{g}{x}\right),$$

$$\lambda_t(x) = 1 - 4\kappa_s\frac{g}{x^2}. \tag{8}$$

For this model x_r, x_t and x_{R_t} are determined numerically. Additionally, there are no restrictions on κ_s in order to produce strong lensing, albeit $y(x_r) \to 0$ as $\kappa_s \to 0$. Therefore, given the scale size of a halo model, there will be a value κ_{smin} such that if $\kappa_s \lesssim \kappa_{smin}$ there will not be strong lensing effects. For the calculations performed in this work a value of $\kappa_{smin} = 0.08$ has been adopted.

2.2.2 *SIS and NSIS models*

The NSIS model is a generalization of the SIS model, with the addition of a core radius to avoid the density singularity in the origin. The NSIS profile is given by

$$\rho(r) = \frac{\sigma_v^2}{2\pi G(r^2+r_c^2)}, \qquad \Sigma(\xi) = \frac{\sigma_v^2}{2\,G\sqrt{\xi^2+r_c^2}}. \tag{9}$$

Choosing $\xi_0 = 4\pi(\sigma_v/c)^2 D_l D_{ls}/D_s$ as the length-scale,[1] $\kappa(x) = 1/(2\sqrt{x^2+x_c^2})$; therefore the deflection angle, γ and eigenvalues are

$$\alpha(x) = \frac{\sqrt{x^2+x_c^2}-x_c}{x},$$

$$\gamma(x) = \frac{x^2 + 2x_c(x_c - \sqrt{x^2+x_c^2})}{2x^2\sqrt{x^2+x_c^2}}$$

$$\lambda_r(x) = 1 + \frac{x_c^2 - x_c\sqrt{x^2+x_c^2}}{x^2\sqrt{x^2+x_c^2}},$$

$$\lambda_t(x) = 1 - \frac{\sqrt{x^2+x_c^2}-x_c}{x^2}. \tag{10}$$

The condition of strong lensing is produced when $x_c < 1/2$. For this model, $x_r = (x_c - (x_c^2 + x_c^{3/2}\sqrt{4+x_c})/2)^{1/2}$ and $x_t = \sqrt{1-2x_c}$. In the regime where $x_c < 1/2$, the area of strong lensing corresponds to $-y_r < y < y_r$; additionally x_{R_t} is obtained from

$$\kappa(x_{R_t}) = \frac{Q_t+1-2x_c-\sqrt{(Q_t+1-2x_c)^2-8(Q_t-1)x_c}}{4(Q_t-1)x_c}, \tag{11}$$

with

$$Q_t = (R_t+1)/(R_t-1) \quad \text{and} \quad \kappa(x_{R_t}) = 1/\left(2\sqrt{x_{R_t}^2+x_c^2}\right).$$

In the SIS (NSIS model with $r_c = 0$) case $x_r = 0, x_t = 1, \alpha(x) = x/|x|$, $\lambda_r(x) = 1$, $\lambda_t(x) = 1 - 1/|x|$, and the condition for strong lensing (multiple images) is in the region $-1 < y < 1$. The parametrization of the images is $y = x - 1$ with magnification $\mu(x) = |x|/||x| - 1|$. For the tangential image $x \epsilon [1, 2]$, $x_{R_t} = R_t/(R_t-1)$ and $y_{R_t} = 1/(R_t-1)$.

[1] For this choice of length-scale $\theta_0 = \xi_0/D_l = 4\pi(\sigma_v/c)^2 D_{ls}/D_s$ corresponds to the Einstein radius for the SIS model ($r_c = 0$).

2.3 Cluster mass

The enclosed mass within radius r ($M(r) = 4\pi\int_0^r r^2\rho(r)\mathrm{d}r$) for each density profile is

$$M_{NFW}(r) = 4\pi\rho_s r_s^3\left(-\frac{x}{1+x} + \ln(1+x)\right),\ x = \frac{r}{r_s} \tag{12a}$$

$$M_{NSIS}(r) = \frac{2\sigma_v^2 r_c}{G}(x - \arctan x),\ x = \frac{r}{r_c}. \tag{12b}$$

As convention, we define the mass M_Δ as that encircled by galaxy cluster when it reaches a radius where its density is a factor Δ of the critical density ρ_{crit}, which is given by

$$\rho_{crit} = \frac{3H^2(z)}{8\pi G} = \rho_{crit,0}E^2(z) \tag{13a}$$

$$\rho_{crit,0} = \frac{3H_0^2}{8\pi G} \approx 1.88\times10^{-29}h^2\ \mathrm{g\ cm^{-3}} \tag{13b}$$

$$E^2(z) = \Omega_m(1+z)^3 + (1-\Omega_m-\Omega_\Lambda)(1+z)^2 + \Omega_\Lambda. \tag{13c}$$

We use two popular choices for the overdensity factor $\Delta = 200$ and $\Delta = \Delta_{vir}$. The virialized overdensity factor is estimated based on the assumption of spherical collapse by $\Delta_{vir}(z) = 178\,\Omega_m(z)^{0.45}$ (e.g. Eke, Navarro & Frenk 1998; Navarro & Steinmetz 2000; Eke, Navarro & Steinmetz 2001). In this last expression, $\Omega_m(z)$ is the matter cosmological parameter as a function of redshift and is given by

$$\Omega_m(z) = \frac{\Omega_m\,(1+z)^3}{E^2(z)}. \tag{14}$$

Defining r_Δ as

$$r_\Delta = \left(\frac{3M_\Delta}{4\pi\Delta\rho_{crit}}\right)^{1/3}, \tag{15}$$

we can find relations between an estimate of the cluster mass such as $M_{vir} \equiv M(r_{vir})$ or $M_{200} \equiv M(r_{200})$, and the parameters that define each of the mass–density profiles.

In the case of the NFW model, choosing $\rho_s = \rho_{crit}\delta_c$,

$$r_s = \frac{r_\Delta}{c_\Delta} \approx \frac{9.51}{c_\Delta}\frac{M_{\Delta15}^{1/3}}{\Delta^{1/3}E(z)^{2/3}}\,h^{-1}\,\mathrm{Mpc},$$

with $M_{\Delta15} = M_\Delta/M_{15}$ ($M_{15} = 10^{15}\,h^{-1}\,\mathrm{M}_\odot$), and using the definition of r_Δ, the following relation holds for the parameters c_Δ and δ_c (Navarro et al. 1996):

$$\delta_c = \frac{\Delta\, c_\Delta^3}{3\,[\ln(1+c_\Delta) - c_\Delta/(1+c_\Delta)]}. \tag{16}$$

Note that c_Δ and δ_c are dimensionless parameters and c_Δ is usually referred as the concentration parameter.[2] In general c_Δ can be expressed as

$$c_\Delta(M_\Delta, z) = c_{\Delta0}M_{\Delta15}^{\alpha_M}(1+z)^{\alpha_z}, \tag{17}$$

where $c_{\Delta0} = c_\Delta(M_{15}, 0)$. Throughout this paper, we will use c_{vir0} to identify $c_{\Delta0}$ when $\Delta = \Delta_{vir}$ and c_{200_0} to recognize $c_{\Delta0}$ when

[2] Originally defined by Navarro et al. (1996) for Δ=200.

$\Delta = 200$. Additionally, unless stated differently, we estimate c_Δ from the ΛCDM N-body simulations Duffy et al. (2008) in the case of relaxed clusters. In these estimations $\alpha_M \approx -0.09$ (independent of Δ), $\alpha_z \approx -0.7$ for $\Delta = \Delta_{\rm vir}$, $\alpha_z \approx -0.4$ for $\Delta = 200$, $c_{\rm vir0} \approx 5.3$ and $c_{200\_0} \approx 3.8$. Observations on the X-ray proprieties of virialized clusters are consistent with the evolution of c_Δ (e.g. Schmidt & Allen 2007), however, these observations in general predict steeper dependences of c_Δ with M_Δ. For example from the works of Buote et al. (2007), Schmidt & Allen (2007) and Ettori et al. (2010), $c_\Delta \propto M_\Delta^{\alpha_M}$ with $\alpha_M \lesssim -0.2$.

For the NSIS model, assuming that $r_\Delta \gg r_{\rm c}$, the velocity dispersion of the cluster is

$$\sigma_v = f_\sigma \sqrt{\frac{M_\Delta G}{2r_\Delta}} = 476 f_\sigma \left(\frac{M_\Delta}{M_{15}}\right)^{1/3} [\Delta(z)E^2(z)]^{1/6} \ {\rm km\ s^{-1}}. \quad (18)$$

Simulations in general do not predict isothermal sphere models; therefore to obtain σ_v we have introduced a factor f_σ, which we choose equal to 0.78 (similar to Bryan & Norman 1998). Through work, for NSIS models we estimate $r_{\rm c}$ as proportional to the virial radius of the cluster (see equation 15), i.e.

$$r_{\rm c}(M_\Delta, z) = r_{\rm c0} \left(\frac{M_{\rm vir}(M_\Delta)}{M_{15}}\right)^{1/3} \left(\frac{E(0)}{E(z)}\right)^{2/3} \left(\frac{\Delta_{\rm vir}(0)}{\Delta_{\rm vir}(z)}\right)^{1/3}, \quad (19)$$

where $M_{\rm vir}(M_\Delta) = (\Delta/\Delta_{\rm vir})^{1/2} M_\Delta$ and $r_{\rm c0}$ is the core radius at $z = 0$ for $M_{\rm vir} = M_{15}$.

2.4 Strong lensing arcs statistics

The total number of arcs produced by a lens (galaxy cluster) with redshift $z_{\rm L}$ depends on numerous parameters. The most important are: parameters from the dark matter profile, the comoving density of the galaxies at $z_{\rm s} > z_{\rm L}$, and the brightness detection limit (size of the telescope). Assuming $n_0(\bar{\mu}, z_{\rm s})$ as the comoving density of galaxies at redshift $z_{\rm s}$, and $\bar{\mu}$ as the image brightness amplification, the total number of detected arcs is obtained by

$$N_{\rm arcs}(M, z_{\rm L}) = \int_{z_{\rm L}}^{z_{\rm max}} n_{\rm o}(\bar{\mu}, z_{\rm s}) \hat{\sigma}_{\rm c}(M, z_{\rm L}, z_{\rm s}) \frac{c{\rm d}t}{{\rm d}z_{\rm s}} (1+z_{\rm s})^3 {\rm d}z_{\rm s}. \quad (20)$$

As in Oguri et al. (2001), we assume that $\bar{\mu} = R_{\rm t}\lambda_{\rm r}^{-2}(x_{\rm t})$ for tangentially elongated images and $\bar{\mu} = R_{\rm r}\lambda_{\rm t}^{-2}(x_{\rm r})$ for radially elongated images (see Appendix A). In equation (20) $z_{\rm max}$ is the maximum redshift assumed for the galaxies, and $c{\rm d}t/{\rm d}z_{\rm s}$ denotes the proper length differential at $z_{\rm s}$, i.e.

$$\frac{c{\rm d}t}{{\rm d}z_{\rm s}} = \frac{c}{H(z_{\rm s})(1+z_{\rm s})} = \frac{c}{H_0 E(z_{\rm s})(1+z_{\rm s})}. \quad (21)$$

Additionally $n_0(\bar{\mu}, z)$ is estimated by

$$n_0(\bar{\mu}, z_{\rm s}) = \int_{\frac{L_{\rm min}}{\bar{\mu}}}^{\infty} \phi(L, z_{\rm s}) {\rm d}L, \quad (22)$$

where $L_{\rm min}(z)$ is the minimum luminosity of a galaxy in order to be detected as an image. Additionally, $\phi(L, z)$ is the comoving density of galaxies which is represented by a Schechter function (Schechter 1976), i.e.

$$\phi(L, z) = \phi^*(z_{\rm s}) \left(\frac{L}{L^*(z_{\rm s})}\right)^{\alpha(z_{\rm s})} \exp\left(\frac{L}{L^*(z_{\rm s})}\right) \frac{{\rm d}L}{L^*(z)}. \quad (23)$$

Therefore, using equation (23) to integrate equation (22) we obtain

$$n_0(\bar{\mu}, z_{\rm s}) = \phi^*(z_{\rm s}) \Gamma \left[1 + \alpha(z_{\rm s}), \bar{\mu}^{-1} \frac{L_{\rm min}(z_{\rm s})}{L^*(z_{\rm s})}\right], \quad (24)$$

where Γ is the incomplete gamma function. In order to express $L_{\rm min}(z_{\rm s})/L^*(z_{\rm s})$ in magnitudes we use

$$M^*(z) = -2.5 \log \frac{L^*(z)}{4\pi(10{\rm pc})^2} + {\rm const}, \ \text{and} \quad (25a)$$

$$m_{\rm lim} = -2.5 \log \frac{L_{\rm min}(z)}{4\pi D_{\rm s}^2 (1+z_{\rm s})^4} + k(z) + {\rm const}, \quad (25b)$$

where $k(z)$ is the k-correction in a given band-pass. Finally, combining equations (25a) and (25b) we get

$$\log\left(\frac{L_{\rm min}(z_{\rm s})}{L^*(z_{\rm s})}\right) = -\frac{2}{5}\{m_{\rm lim} - 5\log\left[D_{\rm s}(1+z_{\rm s})^2\right] - 25 - M^*(z_{\rm s}) - k(z_{\rm s})\}, \quad (26)$$

where $D_{\rm s}$ is in units of Mpc.

2.5 Pseudo-elliptical modelling

In order to estimate the effect of ellipticity in the lens statistics, we partially depart from axially symmetric models using a pseudo-elliptical approach (Golse & Kneib 2002). In order to estimate strong lensing parameters we use

$$\kappa_\epsilon(\boldsymbol{x}) = \kappa(\boldsymbol{x}_\epsilon) + \epsilon \cos 2\phi_\epsilon \ \gamma(\boldsymbol{x}_\epsilon) \quad (27a)$$

$$\gamma_\epsilon^2(\boldsymbol{x}) = \gamma^2(\boldsymbol{x}_\epsilon) + 2\epsilon \cos 2\phi_\epsilon \gamma(\boldsymbol{x}_\epsilon)\kappa(\boldsymbol{x}_\epsilon) + \epsilon^2[\kappa^2(\boldsymbol{x}_\epsilon) - \sin^2 2\phi_\epsilon \gamma^2(\boldsymbol{x}_\epsilon)], \quad (27b)$$

where κ_ϵ and γ_ϵ are κ and γ transformed from the spherically symmetric cases (see e.g. Dúmet-Montoya, Caminha & Makler 2012). These expressions are obtained assuming that the elliptical surface mass distribution depends on $\boldsymbol{x}_\epsilon = \sqrt{x_{1\epsilon}^2 + x_{2\epsilon}^2}$, with $x_{1\epsilon} = \sqrt{a_{1\epsilon}} x_1$, $x_{2\epsilon} = \sqrt{a_{2\epsilon}} x_2$, $\phi_\epsilon = \arctan(x_{2\epsilon}/x_{1\epsilon})$, $a_{1\epsilon} = 1 - \epsilon$ and $a_{2\epsilon} = 1 + \epsilon$. The ellipticity ϵ of the pseudo-elliptical model differs from the standard ellipticity ϵ_Σ expected from a purely elliptical model. From equations (3), (27a) and (27b) we estimate the parameters $\lambda_{\rm t}$ and $\lambda_{\rm r}$ to calculate cross-sections in the image plane. Additionally, we transform these curves to the source plane by using the following transformation:

$$\begin{pmatrix} y_1 \\ y_2 \end{pmatrix} = \begin{pmatrix} x_1 \\ x_2 \end{pmatrix} + \alpha(\boldsymbol{x}_\epsilon) \begin{pmatrix} \sqrt{a_{1\epsilon}} \cos\phi_\epsilon \\ \sqrt{a_{2\epsilon}} \sin\phi_\epsilon \end{pmatrix}, \quad (28)$$

where $\alpha(x)$ is obtained from equation (2). Through this process we compute $\hat{\sigma}_{\rm c}$ and $\bar{\mu}$ in the source plane to estimate the statistics of arcs by using equation (20). For the pseudo-elliptical case $\bar{\mu}$ is averaged as a function of its polar angle in the source plane, i.e.

$$\bar{\mu} = \frac{2R_{\rm t}}{\pi} \int_0^{\pi/2} \lambda_r^{-2}(y_{\rm t}(\phi)) {\rm d}\phi, \quad (29)$$

where $y_{\rm t}$ is the tangential critical curve in the source plane.

The pseudo-elliptical model is a good approximation of an elliptical potential for small values of ϵ. However, at high values of ϵ the mass–density profiles tend to become peanut shaped (as noticed earlier by Golse & Kneib 2002). Using similar analysis as Dúmet-Montoya et al. (2012), we find that the pseudo-elliptical approximation is valid for $\epsilon \lesssim 0.3$ ($\epsilon_\Sigma \lesssim 0.5$) for both the NSIS and NFW models (see Appendix B). Additionally, we confirm (as in Dúmet-Montoya et al. 2012 and Golse & Kneib 2002) that albeit

Table 1. Parameters of the luminosity function used in this work.

Ref.[a]	Redshift	BP	$M_{\rm I}^{*}-5\log h^{b}$	ϕ^{*c}	α
1	0.00–0.45	i'	−21.94	12.8	−1.25
2	0.45–0.81	g'	−22.23	12.2	−1.25
2	0.81–1.11	B	−22.67	11.7	−1.25
2	1.11–1.61	B	−23.01	7.0	−1.25
2	1.61–2.15	u'	−22.62	9.6	−1.07
2	2.15–2.91	u'	−23.42	9.3	−1.07
2	2.91–4.01	u'	−23.49	6.4	−1.07
2	4.01–5.01	u'	−23.84	2.3	−1.07

Notes. [a]Reference of the luminosity function used: (1) Blanton et al. (2001) and (2) Gabasch et al. (2004).
[b]Obtained from the luminosity functions indicated in the first column, transforming $M_{\rm BP}^{*}$ using the following filter transformations: $i'-I=0.68$; $g'-I=1.53$; $B-I=1.88$ and $u'-I=2.69$ (valid for an Sbc galaxy; Fukugita, Shimasaku & Ichikawa 1995).
[c]Units of $10^{-3}\,h^{3}\,{\rm Mpc}^{-3}$.

ϵ is similar to ϵ_{Σ} for low values of ϵ, ϵ is smaller than ϵ_{Σ} in the ranges of ellipticities where the pseudo-elliptical approximation is valid (see Appendix B).

3 RESULTS

Using the assumptions of Section 2 in Section 3.1, we obtain results of the estimated strong lensing number of arcs distribution. Additionally, to clarify the dependence of the arcs statistics with $\hat{\sigma}_{\rm c}$ (see equation 20), in Section 3.2 we perform a cross-sections analysis in Section 3.2. For the results presented in this section we consider the I band. We base the calculation of equation (20) on the luminosity functions of Blanton et al. (2001) ($z<0.45$) and Gabasch et al. (2004) ($z>0.45$). As it can be seen from Table 1, the luminosity function selected is in shorter comoving wavelength band-pass (BP from i' for $z=0.00$–0.45 to u' for $z=4.01$–5.01) as the redshift increases. This is in order to approximately follow the comoving luminosity function of the galaxies that will be detected in the observer-frame I band. We have performed transformations of the band-pass magnitudes taking the expressions found in Fukugita et al. (1995) and using an Sbc as the 'standard galaxy'. The assumed k-correction is from Poggianti (1997); based on this work we have used the following polynomial approximation to obtain the k-correction of an Sbc galaxy

$$k(z_{\rm s})=0.01-0.23z_{\rm s}+1.40z_{\rm s}^{2}-0.50z_{\rm s}^{3}+0.05z_{\rm s}^{4}.$$

For the calculation of equation (20), we adopt $z_{\rm max}=6$ and from hereafter unless stated differently we assume $R_{\rm t}=10$ and $m_{\rm lim}=24$. Additionally, based on the analysis of Oguri et al. (2001), the calculations performed in this section have been corrected for the fact that the background lensed galaxies have a finite size (of radius $r_{\rm gal}$). This is performed by forcing $\hat{\sigma}_{\rm c}(M,z_{\rm L},z_{\rm s})=0$ when $z_{\rm s}$ is such that $\hat{\sigma}_{\rm c}(M,z_{\rm L},z_{\rm s})<\pi\,r_{\rm gal}^{2}$, assuming $r_{\rm gal}=1\,h^{-1}$ kpc.[3] The chosen value of $r_{\rm gal}$ is close to the size of the smallest galaxy observed as an arc (Hattori, Watanabe & Yamashita 1997).

3.1 Number of arcs distribution

Our goal is to study the distribution of $N_{\rm arcs}(z_{\rm L})$ (i.e. equation 20) for a relatively local sample of galaxy clusters ($z_{\rm L}<0.3$). Therefore, we are interested in finding parameters of the dark matter profiles that make an impact on $N_{\rm arcs}$ at relatively low redshifts. An important property of $N_{\rm arcs}(z_{\rm L})$ is the minimum redshift of the lens (galaxy cluster) at which we can detect strong lensing arcs ($z_{\rm cut}$). $z_{\rm cut}$ depends mainly on the mass and on halo parameters that modify the concentration of mass of the cluster near its centre. The approximate parametrical dependencies of $z_{\rm cut}$ can be obtained by assuming $z_{\rm cut}\ll 1$, $z_{\rm cut}\ll z_{\rm s}$, and the limiting value of the parameter that imposes the strong lensing condition. Consequently, for the NFW profile assuming $\kappa_{\rm s}=\kappa_{\rm smin}$ (see Section 2.2.1) we obtain

$$z_{\rm cut}\approx\frac{\kappa_{\rm smin}}{3^{1/3}(4\pi)^{2/3}}\left(\frac{cH_0}{G\,\rho_{\rm crit}^{2/3}}\right)\frac{\Delta_0^{1/3}c_{\Delta}(M_{\Delta},0)}{M_{\Delta}^{1/3}\delta_{\rm c0}}$$
$$\approx 16.8\,\Delta_0^{1/3}M_{\Delta15}^{\alpha_M-1/3}\delta_{\rm c0}^{-1}c_{\Delta0}, \qquad (30)$$

where $\Delta_0=\Delta(z=0)$, $\delta_{\rm c0}=\delta_{\rm c}(z=0)$ and c_{Δ} is obtained through equation (17). Additionally, the expression $\delta_{\rm c0}^{-1}c_{\Delta0}$ is monotonically decreasing function of $c_{\Delta0}$. For the NSIS profile assuming $x_{\rm c}=1/2$ (see Section 2.2.2) we obtain

$$z_{\rm cut}\approx\frac{3^{1/3}}{4^{1/3}\pi^{4/3}}\left(\frac{cH_0}{Gf_{\sigma}^{2}\rho_{\rm crit}^{1/3}}\right)\frac{r_{\rm c}(M_{\Delta},0)}{\Delta_0^{1/3}M_{\Delta}^{2/3}}$$
$$\approx 0.0162\,\Delta_0^{-1/6}M_{\Delta15}^{-1/3}\left(\frac{r_{\rm c0}}{h^{-1}{\rm kpc}}\right), \qquad (31)$$

where in the last step we have used equation (19).

For a fixed mass, variations of the NFW parameter c_{Δ} and the NSIS parameter $r_{\rm c}$ change the fraction of mass encircled at a fixed radius near the centre of the cluster. For low-redshift ($z_{\rm L}\lesssim0.2$) NFW lenses with $M_{\rm vir}=M_{15}$ and $c_{\rm vir0}$ equal to 3 and 8, $M(0.01\,r_{\rm vir})/M_{\rm vir}$ is ≈0.0007 and ≈0.0022, respectively. Additionally, $z_{\rm cut}$ are 0.12 and 0.03, respectively. The SIS profile (i.e. $r_{\rm c}=0$) corresponds to an NSIS profile with maximal encircled mass near the halo centre ($r\ll r_{\rm vir}$) with $z_{\rm cut}=0$. For NSIS ($z_{\rm L}\lesssim0.2$) lenses with mass equal to M_{15} and values of $r_{\rm c0}$ equal 0 and $24\,h^{-1}$ kpc ($r_{\rm c}\approx0.012\,r_{\rm vir}$), $M(0.01\,r_{\rm vir})/M_{\rm vir}$ are ≈0.0100 and ≈0.0017, respectively. Additionally, $z_{\rm cut}$ are 0.00 and 0.20, respectively. In general, changes in parameters that concentrate in the vicinities of the halo centre (at $r\ll r_{\rm vir}$) should shift $z_{\rm cut}$ to lower values. This is expected given that the strong lensing regime in low-redshift clusters is probing their dark matter haloes in the inner regions.[4]

In Fig. 1, we present the number of arcs in the NFW model versus lens redshift. For this figure, the lower-right panel are cases with ellipticity and the rest of the panels correspond to axially symmetric profiles. The upper-left panel corresponds to arcs for dark matter profiles with three different virial masses; $M_{\rm vir}=5\times10^{14}\,h^{-1}\,{\rm M}_{\odot}$, $10^{15}\,h^{-1}\,{\rm M}_{\odot}$ and $2\times10^{15}\,h^{-1}\,{\rm M}_{\odot}$. The upper-right panel corresponds to arcs for dark matter profiles with three different M_{200} masses; $M_{200}=5\times10^{14}\,h^{-1}\,{\rm M}_{\odot}$, $10^{15}\,h^{-1}\,{\rm M}_{\odot}$ and $2\times10^{15}\,h^{-1}\,{\rm M}_{\odot}$. The lower-left panel corresponds to dark matter haloes with $M_{\rm vir}=10^{15}\,h^{-1}\,{\rm M}_{\odot}$, and three values of the concentration parameter at $z=0$ ($c_{\rm vir0}=4.0$, 5.3 and 8). The lower-right panel corresponds to dark matter haloes with $M_{\rm vir}=10^{15}\,h^{-1}\,{\rm M}_{\odot}$, and three values of the ellipticity parameter at $\epsilon=0.00$, 0.15 and 0.30. In the two upper and the lower-right panels we have used $c_{\rm vir}$

[3] It is not expected to find strong lensing effects when the source is bigger or comparable to the strong lensing cross-section (e.g. Schneider et al. 1992).

[4] As an example let us take a simple SIS model. For this case the strong lensing effects will happen inside the Einstein radius which will be at $r_{\rm E}=4\pi(\sigma_v/c)^{2}D_{\rm l}D_{\rm ls}/D_{\rm s}$. If we assume $M_{\rm vir}=M_{15}$ (or $\sigma_v\sim1000\,{\rm kms}^{-1}$) and $z\lesssim0.2$ we obtain $r_{\rm E}\approx400z\,h^{-1}$ kpc, therefore $r_{\rm E}/r_{\rm vir}\lesssim0.2\,z$ for $z\lesssim0.2$.

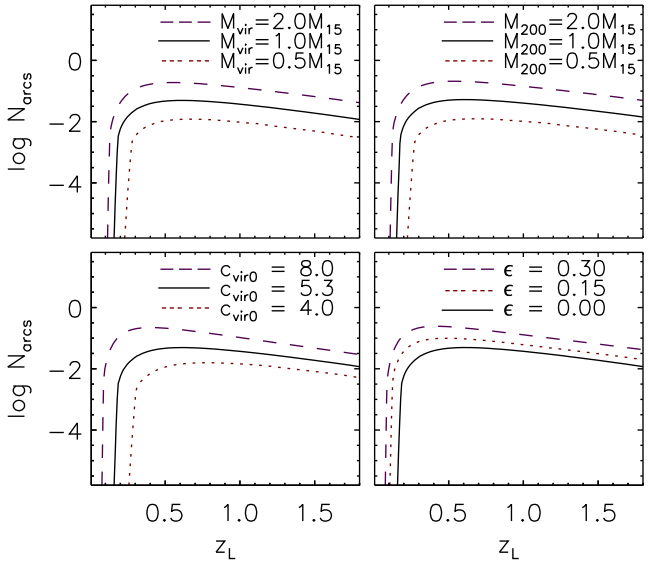

Figure 1. Logarithm of number of arcs versus lens redshift in the NFW model. The upper left (right) corresponds to tangential arcs of galaxy clusters with three different $M_{\rm vir}$ (M_{200}) masses: $5 \times 10^{14}\,h^{-1}\,{\rm M}_{\odot}$ (dotted line), $10^{15}\,h^{-1}\,{\rm M}_{\odot}$ (solid line) and $2 \times 10^{15}\,h^{-1}\,{\rm M}_{\odot}$ (dashed line). For the lower-left panel we generate curves for $c_{\rm vir0} = 4.0$ (dotted line), 5.3 (solid line) and 8.0 (dashed line). For the lower-right panel we generate curves for $\epsilon = 0.00$ (solid line), 0.15 (dotted line) and 0.30 (dashed line). In the two upper and the lower-right panels $c_{\rm vir}$ and c_{200} are from Duffy et al. (2008), in the lower panels $M_{\rm vir} = 10^{15}\,h^{-1}\,{\rm M}_{\odot}$, and in the lower-left panel $c_{\rm vir} \propto (1+z)^{-0.7}$. In all insets $m_{\rm lim} = 24$ and $R_{\rm t} = 10$.

and c_{200} from Duffy et al. (2008), and in the lower-left panel of Fig. 1 we have assumed $c_{\rm vir}(z) = c_{\rm vir0}(1+z)^{-0.7}$.

As seen from Table 2, an increase in the cluster mass affects dramatically the number of arcs, however, this increase just produces a minor shift of $N_{\rm arcs}$ towards lower redshifts. This can be observed as a decrease of $z_{\rm cut}$ from 0.13 to 0.08 and $z_{\rm peak}$ from 0.68 to 0.55 as $M_{\rm vir}$ grows from 0.5 to 2 M_{15} (see Table 2). From the upper panels in Fig. 1, and contrary to our expectations, we find that the statistics of arcs is almost independent on the definition of mass that we are

Table 2. $N_{\rm arcs}(z_{\rm L})$ curve properties in the NFW models.

$M_{\rm vir}{}^a$	$M_{200}{}^a$	$c_{\rm vir0}{}^b$	$c_{200\_0}{}^b$	ϵ	$\epsilon_{\rm g}$	$z_{\rm cut}{}^c$	$z_{\rm peak}{}^c$	Reference for $c_{\Delta}(z)$
0.5	–	5.3	–	0.00	0.00	0.13	0.68	Duffy et al. (2008)
1.0	–	5.3	–	0.00	0.00	0.10	0.60	Duffy et al. (2008)
2.0	–	5.3	–	0.00	0.00	0.08	0.55	Duffy et al. (2008)
–	0.5	–	3.8	0.00	0.00	0.13	0.69	Duffy et al. (2008)
–	1.0	–	3.8	0.00	0.00	0.10	0.61	Duffy et al. (2008)
–	2.0	–	3.8	0.00	0.00	0.07	0.53	Duffy et al. (2008)
1.0	–	4.0	–	0.00	0.00	0.16	0.78	$\propto (1+z)^{-0.7}$
1.0	–	5.3	–	0.00	0.00	0.10	0.61	$\propto (1+z)^{-0.7}$
1.0	–	8.0	–	0.00	0.00	0.05	0.41	$\propto (1+z)^{-0.7}$
1.0	–	5.3	–	0.15	0.00	0.07	0.50	Duffy et al. (2008)
1.0	–	5.3	–	0.30	0.00	0.06	0.42	Duffy et al. (2008)
1.0	–	5.3	–	0.00	0.25	0.10	0.60	Duffy et al. (2008)
1.0	–	5.3	–	0.00	0.50	0.10	0.60	Duffy et al. (2008)

Notes. In these models $m_{\rm lim} = 24$ and $R = 10$.
[a] $M_{\rm vir}$ and M_{200} are given in units of $10^{15}\,h^{-1}\,{\rm M}_{\odot}$.
[b] $c_{\rm vir0}$ and c_{200_0} are defined in Section 2.3.
[c] $z_{\rm cut}$ and $z_{\rm peak}$ are obtained from the curves presented in Fig. 1.

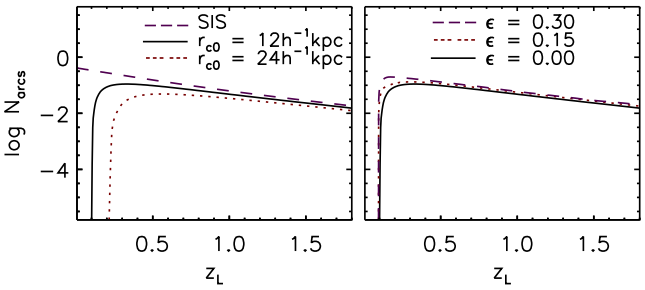

Figure 2. Logarithm of number of arcs model versus lens redshift for the NSIS model. The left-hand panel corresponds to tangential arcs with $r_{\rm c0} = 0$ (SIS model; dashed line), 12 h^{-1} kpc (solid line) and 24 h^{-1} kpc (dotted line). The right-hand panel corresponds to tangential arcs of haloes with $r_{\rm c0} = 12\,h^{-1}$kpc and $\epsilon = 0.00$ (solid line), 0.15 (dotted line) and 0.30 (dashed line). In all insets $M_{\Delta} = 10^{15}\,h^{-1}\,{\rm M}_{\odot}$, $m_{\rm lim} = 24$, $R_{\rm t} = 10$, and the dependence $r_{\rm c}$ with $z_{\rm L}$ is given by equation (19).

Table 3. $N_{\rm arcs}(z_{\rm L})$ curve properties in the NSIS models.

$r_{\rm c0}{}^a$	ϵ	$\epsilon_{\rm g}$	$z_{\rm cut}{}^b$	$z_{\rm peak}{}^b$
0.0	0.00	0.00	0.00	0.00
12.0	0.00	0.00	0.10	0.33
24.0	0.00	0.00	0.20	0.57
12.0	0.15	0.00	0.10	0.26
12.0	0.30	0.00	0.10	0.17
12.0	0.00	0.25	0.10	0.33
12.0	0.00	0.50	0.10	0.33

Notes. For these models: $m_{\rm lim} = 24$, $R = 10$ and $M_{\rm vir} = 10^{15}\,h^{-1}\,{\rm M}_{\odot}$.
[a] In units of h^{-1} kpc.
[b] $z_{\rm cut}$ and $z_{\rm peak}$ are obtained from the curves presented in Fig. 2.

using.[5] This result should be related to departures from the NFW shape in the ΛCDM simulations of Duffy et al. (2008). The curves in the lower-left panel show that the NFW distribution of arcs is strongly sensitive to the concentration parameter. A higher $c_{\rm vir}$ will increase the number of arcs and shift the distributions to lower redshifts. As shown in Table 2, changing the concentration parameter at $z = 0$ from $c_{\rm vir0} = 8$ to 4 increases the redshift where the curves start to rise from $z_{\rm cut} = 0.05$ to 0.16, and where the curves peak from $z_{\rm peak} = 0.41$ to 0.78. From the lower-right panel, we find that an increase in the ellipticity produces a shift of the arc statistics towards lower redshifts. This is reflected in a slight decrease of $z_{\rm cut}$ from 0.10 to 0.06 and a strong decrease of $z_{\rm peak}$ from 0.60 to 0.42 as ϵ increases from 0.0 to 0.3 (see Table 2).

For the NSIS case, we find some important differences in the $N_{\rm arcs}(z_{\rm L})$ curves when $r_{\rm c}$ and ϵ are varied. In Fig. 2, we plot $N_{\rm arcs}(z_{\rm L})$ for dark matter haloes with virial mass $M_{\rm vir} = 10^{15}\,h^{-1}\,{\rm M}_{\odot}$. The left-hand panel of Fig. 2 corresponds to three values of core radius at $z = 0$; $r_{\rm c0} = 0$, 12 and 24 h^{-1} kpc ($\epsilon = 0$). The right-hand panel of Fig. 2 corresponds $r_{\rm c0} = 12\,h^{-1}$ kpc and three different values of ellipticity $\epsilon = 0.00$, 0.15 and 0.30. In general $z_{\rm cut}$ and $z_{\rm peak}$ will be strongly dependent on the core radius ($r_{\rm c}$). This effect is clearly seen in Fig. 2 and Table 3. Increasing $r_{\rm c0}$ from 0 to 24 h^{-1} kpc will increase $z_{\rm cut}$ from 0.00 to 0.20 and $z_{\rm peak}$ from 0.00 to 0.57.

[5] Under the assumption of an NFW profile, for a same halo M_{200} is expected to be lower than $M_{\rm vir}$, since $r_{200} < r_{\Delta}$. Therefore, if we compare two haloes with the same value of mass, the first defined with M_{200} and the second defined with $M_{\rm vir}$, we expect that $N_{\rm arcs}$ is higher in the first.

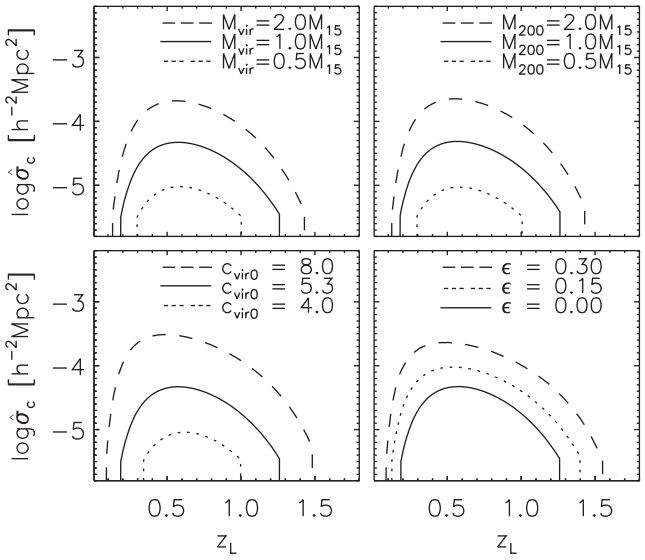

Figure 3. Logarithm of NFW cross-sections (in units of h^{-2} Mpc^2) in function of lens redshift (z_L); the source redshift is fixed to $z_s = 2.0$. Refer to legend in Fig. 1 for details in the selection of parameters to estimate the curves in each panel.

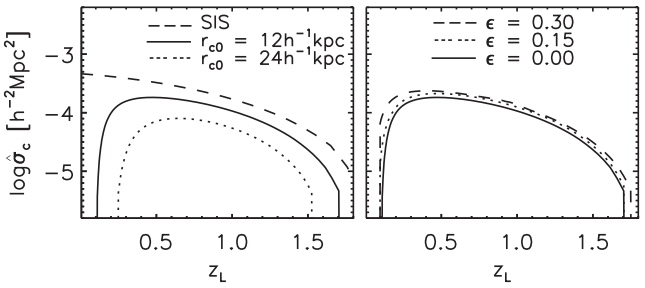

Figure 4. Logarithm of NSIS cross-sections (in units of h^{-2} Mpc^2) in function of lens redshift (z_L); the source redshift is fixed to $z_s = 2.0$. Refer to legend in Fig. 2 for details in the selection of parameters to estimate the curves in each panel.

Additionally, we find that increasing the ellipticity does not change z_{cut}, but produces a preferential enhancement on the arc statistics at redshifts close to z_{cut}. In particular, as seen in Fig. 2 and Table 3, for a dark matter profile with $M_{vir} = 10^{15}\,h^{-1}\,M_\odot$, $r_{c0} = 12\,h^{-1}$ kpc, when ϵ increases from 0.0 to 0.3, z_{peak} decreases from 0.33 to 0.17.

3.2 Strong lensing cross-section

From equation (20), we expect that parameters derived from $N_{arcs}(z_L)$ (like e.g. z_{cut} and z_{max}) are mostly influenced by the lensing cross-section. To show this effect we have calculated cross-sections in the source plane with a fixed source redshift. We have plotted the cross-sections as a function of lens redshift (z_L), in the NFW model (Fig. 3) and NSIS model (Fig. 4), respectively. In both figures we have assumed that the redshift of the source is $z_s = 2$.

As in the case of the number of arcs (Section 3.1), for NFW models, we have varied some parameters of the lens halo (Fig. 3) like M_Δ (upper-left panel), M_{200} (upper-right panel), concentration parameter (c_Δ) (lower-right panel), and ϵ (lower-left panel). From the upper panels of Fig. 3, we confirm that the effect of changing the mass in the NFW model is analogous to what we see in N_{arcs} (Fig. 1, Section 3.1). In the lower-left panel of Fig. 3, we find that for an NFW halo with $M_{vir} = 10^{15}\,h^{-1}\,M_\odot$, the minimum redshift at which the cross-sections become non-negligible grows from 0.09 to ∼0.33 and the redshift at which the cross-sections are peaking grows from 0.49 to 0.62 as c_Δ decreases from 8 to 4. From the lower-right panel of Fig. 3, we find that increasing the ellipticity decreases the minimum redshift at which the cross-sections become non-negligible and the redshift at which the cross-sections are peaking. Consequently, increasing ellipticity produces a preferential enhancement of the cross-section close to redshifts where it starts to be non-negligible. These results are analogous to those found in the discussion of N_{arcs} in function of z_L depicted in Fig. 1.

In the case of the NSIS profiles, the cross-sections (Fig. 4) are strongly dependent on the core radius (r_c). As r_c increases, the cross-sections decrease in size and in redshift range. For an NSIS halo with $M_{vir} = 10^{15}\,h^{-1}\,M_\odot$, if r_c increases from 0 to 24 h^{-1} kpc, the minimum redshift at which the cross-sections start to be non-negligible grows from ∼0.00 to ∼0.25. Additionally, increasing the ellipticity will produce a preferential enhancement of the cross-section at the redshift where they start to be non-negligible. These results are similar to those in $N_{arcs}(z_L)$ for NSIS models (see Fig. 2 and Section 3.1). For a fixed z_s different than two, the cross-sections of both the NFW and NSIS profile will have similar overall shape to those presented in Figs 3 and 4. However, the maximum redshift at which these curves are non-negligible will increase or decrease accordingly with a z_s greater or lower than two. Our cross-sections estimations (for $z_s = 1$) are similar to those found in Fig. 1 of Meneghetti, Bartelmann & Moscardini (2003). These calculations (with $\Delta = 200$) were confirmed by assuming a constant concentration parameter c_{200} in the NFW model and $f_\sigma \sim 0.7$ in the SIS model.[6]

3.3 Additional effects in the arc distribution

In Section 2, we have assumed that the galaxy clusters (lenses) are a dark matter potential with elliptical symmetry. Additionally, as described in the beginning of this section, our calculations have been performed considering that the galaxies behind the lenses have finite size. These simplifications minimize the number of free parameters required in our formulation. However, in order to find the limitations of this approach, we need to estimate the effect produced by some parameters that have been ignored. In this section, we estimate the variation of the number of arcs as a function of the ellipticity of the lensed galaxies based on Keeton (2001). In the end of this section, we also include comments about other parameters that could be relevant for our calculations.

The dependence of the number of arcs on the ellipticity of the lensed galaxies is shown in Fig. 5. In this figure we present the number of arcs in function of z_L for NFW (left-hand panel) and NSIS (right-hand panel) dark matter profiles with virial mass $M_{vir} = M_{15}$. In each panel of this plot we have used three different values for the ellipticity of the lensed galaxies, $e_g = 0.00, 0.25$ and 0.50. From this figure we see a slight increase in the number of arcs as a function of the lensed galaxies ellipticity. From Fig. 5 and Tables 2 and 3, we conclude that increasing the lensed galaxy ellipticity increases the number of arcs, however it does not change the overall shape of $N_{arcs}(z_L)$.

[6] In Meneghetti et al. (2003), the authors calculate cross-sections using the SIS (NSIS with $r_c = 0$) and NFW model.

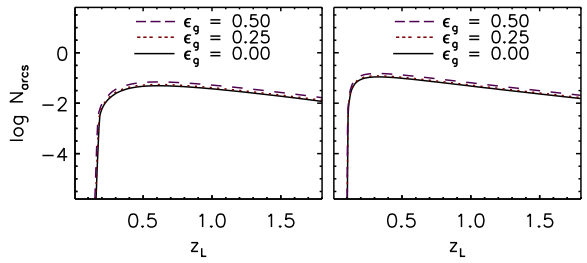

Figure 5. Effect of the lensed galaxy ellipticity in in $N_{\rm arcs}$. The left-/right-hand panels correspond to the NFW and NSIS axially symmetric dark matter profiles. The curves in both panels are obtained with $M_{\rm vir} = 10^{15}\,h^{-1}\,{\rm M}_{\odot}$, $m_{\rm lim} = 24$, $R_{\rm t} = 10$ and three different lensed galaxies ellipticities $\epsilon_{\rm g} = 0.00$ (solid line), 0.25 (dotted line) and 0.50 (dashed line). In the left-hand panel $c_{\rm vir}$ is from Duffy et al. (2008) and in the right-hand panel $r_{\rm c0} = 12\ h^{-1}$ kpc (the dependence $r_{\rm c}$ with $z_{\rm L}$ is given by equation 19).

The effect of the seeing will be to circularize the object image, therefore larger seeing will decrease the number of arcs. This effect has been explored by Cypriano et al. (2001), and their conclusion was that for a seeing of $\gtrsim$1.5 arcsec we expect a decrease in the $N_{\rm arcs}$ by a factor close to one order of magnitude. In a survey where the seeing is $\lesssim$1.0 arcsec and is not varying significantly between observations, we expect that this effect will not be important in affecting the shape and amplitude of the distribution of the number of arcs.

There are other effects that could be affecting the statistics of arcs that are out of the scope of this paper. Among them are: the triaxiality on the lens mass distribution (Oguri, Lee & Suto 2003), cluster mergers (Torri et al. 2004), halo concentration distribution (Fedeli et al. 2007), cluster asymmetries and substructures (Meneghetti et al. 2007), influence of stellar mass in galaxies (Hilbert et al. 2008), and baryonic cooling (Rozo et al. 2008; Wambsganss, Ostriker & Bode 2008). Although most of these effects will affect substantially the lens statistics, it is expected that the shape of $N_{\rm arcs}(z_{\rm L})$ will be robust for low-redshift clusters ($z_{\rm L} \lesssim 0.3$). This is because at low redshift $N_{\rm arcs}(z_{\rm L})$ is mostly dependent on the encircled mass near the centre of the mass distribution of the lens. Note though that the baryonic matter contribution could be important in the inner regions of the clusters. However, latest studies suggest that pure dark matter models (like the ones used in this work) could be enough to describe cluster haloes even in those regions where baryonic matter is important (Newman et al. 2013b,a). Future work with more complex lens models will be helpful to understand better the power of the simplified methodology used in this work. In the next section, we briefly describe how to apply this formulation to an ensemble of low-redshift galaxy clusters. Through this approach, we expect to obtain first-order constrains on parameters that have an impact on the encircled mass at $r \ll r_{\Delta}$.

3.4 KS test to an ensemble of galaxy clusters

To give applicability to our method, the mass of the cluster (M_{Δ}) must be related to some observable parameter. For this purpose, we use the empirical relation between the X-ray luminosity of the clusters and M_{200} (i.e. $\Delta = 200$) obtained by Leauthaud et al. (2010), which can be expressed as

$$M_{200}(L_{\rm X}, z) = \frac{B^*}{E(z)} \left(\frac{L_{\rm X} E(z)^{-1}}{10^{44}\ h^{-2}\ {\rm erg\ s^{-1}}} \right)^{A^*} 10^{15}\, h^{-1}\, {\rm M}_{\odot}, \qquad (32)$$

where $L_{\rm X}$ is the X-ray luminosity in the 0.1–2.4 keV band, $A^* \approx 0.64$, and $B^* \approx 0.400$.[7]

We apply our results to a real case by compiling the information of masses and presence of arcs in a large sample of galaxy clusters. We selected bright X-ray Abell clusters ($L_{\rm X} > 1.2 \times 10^{44}\,h^{-2}$ erg s^{-1} or $M_{200} \gtrsim 5 \times 10^{14}\,h^{-1}\,{\rm M}_{\odot}$) in the Southern hemisphere ($-50^{\circ} \leq \delta \leq 15^{\circ}$) with $z \geq 0.05$. The clusters were observed with the FORS1 instrument mounted on the VLT-Antu telescope. The requirement that $z \geq 0.05$ was to ensure that a large fraction of the clusters fits inside the field-of-view (FOV) of the camera (6.8 arcmin × 6.8 arcmin). The observations were obtained under homogeneous sky conditions and sub-arcsecond image quality (median of 0.6 arcsec). The complete sample consists of 49 clusters (see Table 4) and the weak lensing properties of 24 of them have been previously presented in (Cypriano et al. 2004, see here also for details on the data reduction). The pixel scale used was 0.2 arcsec and the FOV length of 6.8 arcmin corresponds to proper distances of ≈0.3, 0.7 and 1.3 h^{-1} Mpc for small ($z = 0.05$), average ($z = 0.14$) and large ($z = 0.3$) clusters redshifts. The V, R, I bands imaging was centred on the cluster cores and with exposures times of 330 s in each filter. In our search of strong lensing images, we found that 8 out of 49 clusters show strong lensing arcs (see Table 4 and Appendix C) and Fig. 6; the minimum redshift at which we found arcs was ≈0.08.

We estimate the observed cumulative number of clusters with arcs on our sample as a function of their redshift, and compare this with the expected cumulative number of clusters with arcs from our models. Based on Duffy et al. (2008) for virialized clusters, in the case of the NFW model, we estimate the clusters concentration parameters using equation (17) with $\alpha_M = -0.091$ and $\alpha_z = -0.44$. In the case of the NSIS model, we parametrize the core radii using equation (19) with $M_{\rm vir} = (200/\Delta_{\rm vir}(z_{\rm L}))^{1/2} M_{200}$. The assumed I-band limiting magnitude is $m_{\rm lim} = 24$, which is close to the sensitivity limit of our observations. However, the estimated cumulative number of clusters with arcs is insensitive to the limiting magnitude in the range $22 \lesssim m_{\rm lim} \lesssim 26$. The assumed value of $R_{\rm t}$ is 10 albeit the cumulative distributions are also not affected for $5 \lesssim R_{\rm t} \lesssim 20$. Similar conclusions are obtained when we vary the ellipticity of the lensed galaxies from $\epsilon_{\rm g} = 0$ to $\epsilon_{\rm g} = 0.5$. In general, the cumulative distributions should be not affected by any additional parameter that does not change appreciably the shape of $N_{\rm arcs}(z_{\rm L})$.

The observed cumulative number of clusters with arcs of our Abell cluster sample has been compared with six different prescriptions of each NFW model (Fig. 7) and NSIS model (Fig. 8), respectively. The three model curves presented in the left-hand panel of Fig. 7 correspond to axially symmetric NFW profiles with $c_{200\_0} =$ 6.5, 15 and 800, respectively. The three model curves shown in the right-hand panel Fig. 7 correspond to pseudo-elliptical NFW profiles with $\epsilon = 0.3$ and $c_{200\_0} = 4.4$, 10 and 800, respectively. Note that a value of the pseudo-elliptical ellipticity $\epsilon = 0.3$ correspond to a value of $\epsilon_{\Sigma} \sim 0.5$ (see Section 2.5 and Appendix B). This particular value of ϵ_{Σ} is close to estimations based on weak and strong lensing of the sample presented in Oguri et al. (2012). The three model curves shown in the left-hand panel of Fig. 8 correspond to axially symmetric NSIS profiles with $r_{\rm c0} = 0$ (SIS), 5 and 12 h^{-1} kpc, respectively. The three model curves presented

[7] The original expression presented in Leauthaud et al. (2010) is $M_{200}E(z) = M_0 B(L_{\rm X}E(z)^{-1}/L_{X0})^A$, where $M_0 = 10^{13.7} h_{72}^{-1}\ {\rm M}_{\odot}$, $L_{X0} = 10^{42.7} h_{72}^{-2}$ erg s^{-1} and h_{72} is H_0 in units of 72 kms^{-1} Mpc^{-1}. The values of $A^* \approx 0.64$, and $B^* \approx 0.400$ in equation (32) are obtained rewriting this equation with $A = 0.64$ and $\log B = 0.03$.

Table 4. Abell clusters observed with VLT. Col. (1): cluster name. Cols (2) and (3): optical positions in J2000.0 equatorial coordinates. Col. (4): redshift. Col. (5): redshift reference. Col. (6): 0.1–2.4 keV absorption corrected flux in units of 10^{-12} erg cm^{-2} s^{-1} (from Ebeling et al. 1996). Col. (7): $\log L_X$, where L_X is the 0.1–2.4 keV luminosity in units of $E(z)\,h^{-2}$ erg s^{-1}. Col. (8): $\log M_{200}$, where M_{200} is in units of $E(z)^{-1}\,h^{-1}\,M_\odot$. Col. (9): yes, if the cluster presents evidence of strong lensing images, no otherwise (see Appendix C for details).

Object name (1)	$\alpha_{2000.0}$ (2)	$\delta_{2000.0}$ (3)	z (4)	Ref (5)	f_X (6)	$\log L_X$ (7)	$\log M_{200}$ (8)	Arcs? (9)
A0022	5.161	−25.7220	0.1424	8	7.3	44.20	14.73	No
A0085	10.453	−9.318 00	0.0551	5	72.3	44.37	14.84	No
A0141	16.388	−24.6500	0.2300	2	5.7	44.50	14.92	No
A0399	44.457	13.0530	0.0718	5	29.0	44.21	14.73	No
A0401	44.737	13.5730	0.0737	5	42.6	44.40	14.86	No
A0478	63.359	10.4660	0.0881	2	39.1	44.51	14.93	No
A0520	73.531	2.920 00	0.1990	2	8.3	44.54	14.95	No
A0545	83.097	−11.5360	0.1540	2	9.2	44.37	14.84	No
A0644	124.355	−7.528 00	0.0704	2	36.8	44.29	14.79	No
A0750	137.299	10.9890	0.1800	2	8.4	44.46	14.90	No
A0754	137.256	−9.655 00	0.0542	2	64.1	44.31	14.80	No
A0780	139.528	−12.0990	0.0539	2	48.4	44.18	14.72	No
A0795	141.024	14.1680	0.1359	2	7.1	44.15	14.70	No
A0901	149.122	−9.948 00	0.1700	4	5.2	44.21	14.73	No
A0907	149.589	−11.0610	0.1527	1	8.1	44.31	14.80	Yes
A1084	161.128	−7.084 00	0.1323	8	9.7	44.26	14.77	Yes
A1285	172.586	−14.5750	0.1061	2	11.2	44.13	14.69	No
A1300	172.979	−19.9140	0.3072	2	6.1	44.77	15.10	No
A1437	180.106	3.351 00	0.1345	8	10.2	44.30	14.79	No
A1451	180.811	−21.5270	0.1711	1	6.5	44.31	14.80	Yes
A1553	187.700	10.5560	0.1652	2	6.1	44.25	14.76	No
A1650	194.674	−1.756 00	0.0838	8	25.6	44.29	14.79	No
A1651	194.850	−4.189 00	0.0849	8	27.1	44.32	14.81	No
A1664	195.934	−24.2560	0.1283	8	7.8	44.14	14.69	No
A2029	227.729	5.720 00	0.0773	5	61.6	44.60	14.98	Yes
A2104	235.027	−3.306 00	0.1533	8	7.7	44.29	14.79	Yes
A2163	243.956	−6.150 00	0.2030	2	21.0	44.96	15.22	Yes
A2204	248.195	5.574 00	0.1522	8	21.2	44.72	15.06	Yes
A2345	321.744	−12.1410	0.1765	2	7.6	44.40	14.86	No
A2384	328.069	−19.6000	0.0943	2	18.2	44.24	14.76	No
A2426	333.635	−10.3650	0.0978	2	12.2	44.10	14.67	No
A2597	351.319	−12.1240	0.0852	2	25.9	44.31	14.80	No
A2744	3.567	−30.3830	0.3080	2	5.7	44.75	15.08	Yes
A2811	10.533	−28.5360	0.1079	9	10.9	44.14	14.69	No
A3017	36.485	−41.9060	0.2195	3	6.2	44.50	14.92	No
A3041	40.333	−28.6870	0.2352	10	5.3	44.49	14.92	No
A3112	49.485	−44.2380	0.0753	9	36.4	44.35	14.82	No
A3292	72.459	−44.6860	0.1723	1	6.8	44.33	14.82	No
A3364	86.906	−31.8720	0.1483	3	8.6	44.31	14.80	No
A3378	91.470	−35.3010	0.1410	1	8.2	44.24	14.76	No
A3396	97.205	−41.7250	0.1759	3	5.4	44.25	14.76	No
A3411	130.475	−17.4930	0.1687	6	10.5	44.50	14.92	No
A3444	155.953	−27.2640	0.2533	2	8.6	44.76	15.09	No
A3695	308.694	−35.8300	0.0894	2	15.1	44.11	14.67	No
A3739	316.073	−41.3390	0.1651	7	6.2	44.26	14.77	No
A3856	334.656	−38.8870	0.1379	2	9.5	44.29	14.79	No
A3888	338.637	−37.7330	0.1529	8	15.2	44.58	14.97	No
A3984	348.907	−37.7480	0.1805	2	6.9	44.38	14.84	No
A4010	352.809	−36.5020	0.0955	9	14.1	44.14	14.69	No

Note. References: (1) Ebeling et al. (1996); (2) Struble & Rood (1999); (3) De Grandi et al. (1999); (4) Schindler (2000); (5) Oegerle & Hill (2001); (6) Ebeling, Mullis & Tully (2002); (7) Böhringer et al. (2004); (8) Pimbblet et al. (2006); (9) Zaritsky, Gonzalez & Zabludoff (2006); (10) Coziol et al. (2009).

in the right-hand panel of Fig. 8 correspond to pseudo-elliptical NSIS profiles with $\epsilon = 0.3$ with $r_{c0} = 0$ (SIS), 8 and 16 h^{-1} kpc, respectively.

The Kolmogorov-Smirnov (KS) test is used to verify if the null hypothesis that the observed number of arcs comes from the same distribution than those estimated from the models. In the panels of Fig. 7, the curves with extreme values of c_{200_0} correspond to cases where the predicted cumulative distributions depart significantly from the observed (≈95 per cent level of confidence). In the panels of Fig. 8, the only curves that depart significantly form the observed are those with the maximum value of r_{c0}. In consequence, we conclude that we reject the null hypothesis at a confidence level

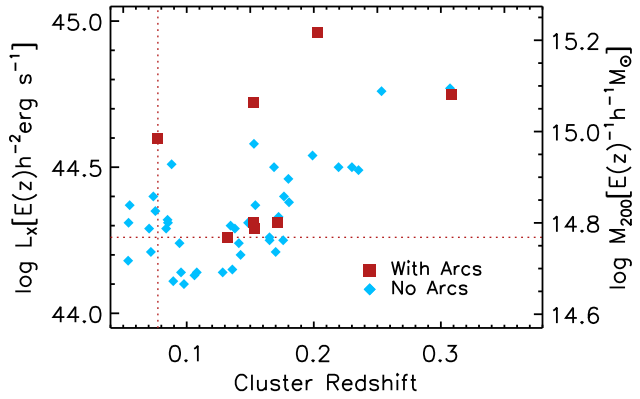

Figure 6. L_X as a function of redshift for our bright sample of Abell clusters. Squares and diamonds are cluster with and without evidence of arcs, respectively. Vertical and horizontal dotted lines are used to mark the minimum redshift and minimum X-ray luminosity of clusters that present gravitational arcs.

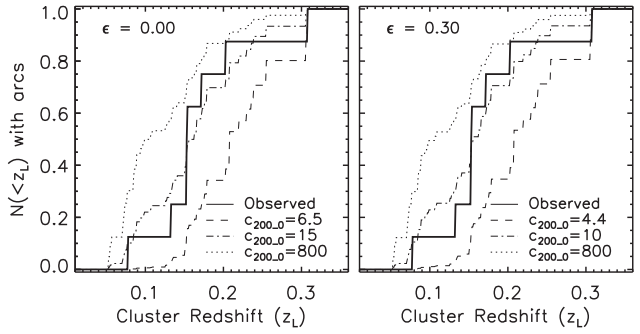

Figure 7. Observed cumulative distribution of a sample of Abell clusters with arcs as a function of cluster redshift (solid line in both panels). Left-hand panel: axially symmetric NFW models ($\epsilon = 0$) with concentration parameters of $c_{200\_0} = 6.5$ (dashed line), 15 (dash–dotted line) and 800 (dotted line). Right panel: NFW pseudo-elliptical models with $\epsilon = 0.3$ and concentration parameters of $c_{200\_0} = 4.4$ (dashed line), 10 (dash–dotted line) and 800 (dotted line). In all insets $m_{\rm lim} = 24$, $R_{\rm t} = 10$ and the dependence of c_{200} on M_{200} and $z_{\rm L}$ is given by equation (17).

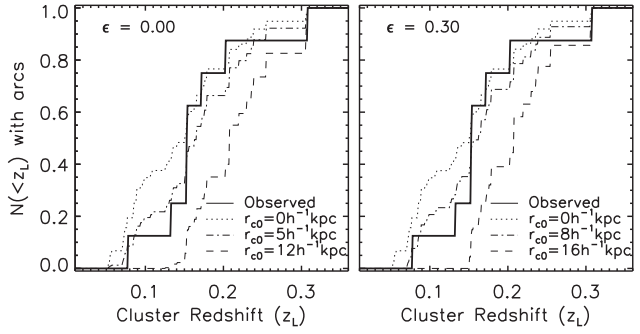

Figure 8. Observed cumulative distribution of a sample of Abell clusters with arcs as a function of cluster redshift (solid line both panels). Left-hand panel: axially symmetric NSIS models ($\epsilon = 0$) with core radii of $r_{\rm c0}\,[\,{\rm h}^{-1}\,{\rm kpc}] = 0$ (SIS; dotted line), 5 (dash–dotted line) and 12 (dashed line). Right-hand panel: NSIS pseudo-elliptical models with $\epsilon = 0.3$ and core radii of $r_{\rm c0}\,[{\rm h}^{-1}\,{\rm kpc}] = 0$ (SIS: dotted line), 8 (dash–dotted line) and 16 (dashed line). In all insets $m_{\rm lim} = 24$, $R_{\rm t} = 10$ and the dependence of $r_{\rm c}$ on M_{200} and $z_{\rm L}$ is given by equation (19).

>95 per cent for $c_{200\_0} \lesssim 6.5$ and $c_{200\_0} \gtrsim 800$ in cases of NFW profiles without ellipticity and for $c_{200\_0} \lesssim 4.4$ and $c_{200\_0} \gtrsim 800$ in cases of NFW profiles with ellipticity ($\epsilon = 0.3$). Additionally, we reject the null hypothesis at a confidence level >95 per cent for $r_{\rm c0} \gtrsim 12\,h^{-1}$ kpc and for $r_{\rm c0} \gtrsim 16\,h^{-1}$ kpc in cases of NSIS profiles without and with ellipticity ($\epsilon = 0.3$), respectively. Note that although incrementing the ellipticity does not significantly affect $z_{\rm cut}$, it preferentially enhances the statistics of clusters at low redshifts (as described in Section 3.1). Therefore, when we compare axially symmetric models to cases where ellipticity is taken into account, we obtain clear differences on the constraints on c_{200_0} or $r_{\rm c0}$. Based on expressions (30) and (31) the estimations of c_{200_0} and $r_{\rm c0}$ allow us to calculate approximate values of $z_{\rm cut}$ for clusters with masses within those on our sample. If we assume $M_{200} = 10^{\langle \log M_{200} \rangle} \approx 0.62\,M_{15}$ with $\langle \log M_{200} \rangle$ the logarithm averaged cluster mass, we find that $z_{\rm cut} \lesssim 0.07$ for NFW profiles and $z_{\rm cut} \lesssim 0.12$ for NSIS.

As a reference, the results from ΛCDM simulations of Duffy et al. (2008) indicate that $c_{200\_0} \approx 3.8$ ($\sigma_{\log c} \sim 0.12$). Hence, although we find more concentrated haloes ($c_{200\_0} \gtrsim 4.4$) than those of Duffy et al. (2008), our expected values of c_{200_0} fall within the predicted errors of the simulations. The concentrations found in this work are also consistent with $c_{200\_0} \sim 5.4$ as predicted by N-body ΛCDM simulations of Prada et al. (2012).[8] Note that larger strong lensing surveys on clusters at low redshift can provide better constraints on cumulative distribution of clusters with arcs, and thus, more restrictive values on c_{200_0}, $r_{\rm c0}$ and $z_{\rm cut}$. For example, including clusters with $z \lesssim 0.05$ in our sample should decrease our estimations on the upper limit of c_{200_0} for NFW profiles and/or increase the lower limit of $r_{\rm c0}$ for NSIS profiles.

As mentioned in Section 3.3, there are many effects not considered in our approach that could have an influence on our results. In particular, selecting a sample of massive (X-ray bright) and low-redshift clusters expected to be mostly relaxed and virialized, and therefore, with more concentrated mass profiles than normal populations of galaxy clusters (e.g. Rasia et al. 2013). Additionally, strong lensing should be preferably observed in clusters where the line of sight is oriented along the main axis of their triaxial mass profiles (e.g. Clowe, De Lucia & King 2004; Gavazzi 2005; Oguri et al. 2005). The selection effects in consideration could be artificially increasing the observed concentration up to 30 per cent (e.g. Oguri et al. 2012; Meneghetti et al. 2014; Merten et al. 2015). Considerations of these type should be analysed in future studies by using more complex models than those in this work.

4 SUMMARY AND CONCLUSIONS

In this paper, we introduce an axially symmetric formula (equation 20) to calculate the probability of finding strong lensing arcs in galaxy clusters as a function of their redshift and virial mass. This formula has been modified in order to include ellipticity through the use of a pseudo-elliptical approximation. We have tested this formulation using the NFW and NSIS dark matter mass profiles, and we have studied its dependence on the mass, core radius, concentration parameter and ellipticity.

For the NFW profiles, we have confirmed that the halo cluster masses produce important variation on the number of arcs detected.

[8] Prada et al. (2012) estimate higher concentration parameters at masses in the range of galaxy clusters than previous ΛCDM simulations. This result is attributed to the fact that Prada et al. (2012) find little evolution on massive haloes, and as a consequence, higher concentrations than previous studies.

Incrementing by a factor of four the halo cluster mass will increase the number of arcs in approximately an order of magnitude. However, such increment in mass does not change significantly the shape of the number of arcs distributions as a function of redshift. In this model, changes in the concentration parameter produce substantial variations in the number of arcs as a function of the cluster redshift. In particular, for an NFW profile with virial mass $\sim 10^{15}\, h^{-2}\, \mathrm{M}_{\odot}$, a change in the concentration parameter normalization ($c_{\Delta 0}$) from 4 to 8 will shift the minimum cluster redshift where we find arcs from $z_{\rm cut} \sim 0.16$ to 0.05. Such change will also vary the redshift where the $N_{\rm arcs}$ are maximum from $z_{\rm peak} \sim 0.8$ to 0.4.

In the case of the NSIS models, the distribution of the arcs is very sensitive to the core radius of the model. In particular, for an NSIS profile with virial mass $\sim 10^{15}\, h^{-2}\, \mathrm{M}_{\odot}$, a core radius ranging from 0 to 24 h^{-1} kpc will produce dramatic variations on the lens statistics. For this case, the minimum redshift where we find arcs is shifted from $z_{\rm cut} \sim 0.0$ to 0.2, and the redshift where the $N_{\rm arcs}$ are maximum vary from $z_{\rm peak} \sim 0.0$ to 0.6. In both dark matter profiles studied in this work, we find that an increase in ellipticity does not significantly change $z_{\rm cut}$, however, it produces a preferential enhancement on the arc statistics at redshifts close to $z_{\rm cut}$. This effect is clearly observed through a strong decrease of $z_{\rm peak}$ as the ellipticity of the dark matter potential increases. Therefore, the ellipticity has an important impact on the statistics of arcs.

We have implemented our method to analyse the arc statistics of an X-ray bright low-redshift sample of Abell clusters that were observed with VLT. Through a simple KS test, we have been able to constrain the concentration parameter for NFW profiles and the core radius for NSIS profiles. For NFW profiles, we obtain that $c_{200\_0} \geq 6.5$ for axially symmetric profiles, and $c_{200\_0} \geq 4.4$ for elliptical profiles. Consequently, our estimations of the concentration are consistent with those predicted by N-body ΛCDM simulations (within the rms errors). Additionally, for NSIS profiles, our Abell cluster arc statistics provide upper limits on the core radius ($r_{\rm c0} \leq 16\, h^{-1}$ kpc) and thus an SIS model is not ruled out from our observations.

For an arbitrary density profile, our approach should be useful to estimate parameters that modify the mass distribution near the halo centre ($r \ll r_{\Delta}$). These parameters are related with the lowest cluster redshift where strong arcs can be observed ($z_{\rm cut}$) for a well-defined sample of galaxy clusters. Such lowest redshift is expected to lie in the range 0.0–0.2, highlighting the need to adopt a very low-z limit for samples to study the clusters mass profiles.

ACKNOWLEDGEMENTS

We thank the anonymous referee for his/her insightful comments that helped us improve this work. JPK acknowledges support from the ERC advanced grant LIDA and from CNRS. LSJ is partially supported by FAPESP (project 2012/00800-4) and CNPq. ESC is partially supported by FAPESP(2014/13723-3) and CNPq. LEC received partial support from the Center of Excellence in Astrophysics and Associated Technologies (PFB06) and from CONICYT Anillo project ACT-1122. CS acknowledges support from CONICYT-Chile (FONDECYT 3120198 and Becas Chile 74140006). Based on observations made with ESO Telescopes at the La Silla Paranal Observatory under programme IDs 67.A-0597(A) and 70.B-0440(A).

REFERENCES

Bartelmann M., Steinmetz M., Weiss A., 1995, A&A, 297, 1
Bartelmann M., Huss A., Colberg J. M., Jenkins A., Pearce F. R., 1998, A&A, 330, 1
Beraldo e Silva L. J., Lima M., Sodré L., 2013, MNRAS, 436, 2616
Blanton M. R. et al., 2001, AJ, 121, 2358
Böhringer H. et al., 2004, A&A, 425, 367
Bryan G. L., Norman M. L., 1998, ApJ, 495, 80
Buote D. A., Gastaldello F., Humphrey P. J., Zappacosta L., Bullock J. S., Brighenti F., Mathews W. G., 2007, ApJ, 664, 123
Campusano L. E., Kneib J.-P., Hardy E., 1998, ApJ, 496, L79
Campusano L. E., Cypriano E. S., Sodré L., Jr, Kneib J.-P., 2006, in Mamon G. A., Combes F., Deffayet C., Fort B., eds, EAS Publ. Ser. Vol. 20, Mass Distribution and Dynamical State of Galaxy Clusters in the LZLS Sample. ESA, EDP Sciences, France, p. 269
Clowe D., De Lucia G., King L., 2004, MNRAS, 350, 1038
Cooray A. R., 1999, ApJ, 524, 504
Coziol R., Andernach H., Caretta C. A., Alamo-Martínez K. A., Tago E., 2009, AJ, 137, 4795
Cypriano E. S., Sodré L., Jr, Campusano L. E., Kneib J.-P., Giovanelli R., Haynes M. P., Dale D. A., Hardy E., 2001, AJ, 121, 10
Cypriano E. S., Sodré L., Jr, Kneib J.-P., Campusano L. E., 2004, ApJ, 613, 95
De Grandi S. et al., 1999, ApJ, 514, 148
Duffy A. R., Schaye J., Kay S. T., Dalla Vecchia C., 2008, MNRAS, 390, L64
Dúmet-Montoya H. S., Caminha G. B., Makler M., 2012, A&A, 544, A83
Ebeling H., Voges W., Bohringer H., Edge A. C., Huchra J. P., Briel U. G., 1996, MNRAS, 281, 799
Ebeling H., Mullis C. R., Tully R. B., 2002, ApJ, 580, 774
Eke V. R., Navarro J. F., Frenk C. S., 1998, ApJ, 503, 569
Eke V. R., Navarro J. F., Steinmetz M., 2001, ApJ, 554, 114
Ettori S., Gastaldello F., Leccardi A., Molendi S., Rossetti M., Buote D., Meneghetti M., 2010, A&A, 524, A68
Fedeli C., Bartelmann M., Meneghetti M., Moscardini L., 2007, A&A, 473, 715
Fukugita M., Shimasaku K., Ichikawa T., 1995, PASP, 107, 945
Gabasch A. et al., 2004, A&A, 421, 41
Gao L., Navarro J. F., Frenk C. S., Jenkins A., Springel V., White S. D. M., 2012, MNRAS, 425, 2169
Gavazzi R., 2005, A&A, 443, 793
Gavazzi R., Fort B., Mellier Y., Pelló R., Dantel-Fort M., 2003, A&A, 403, 11
Gladders M. D., Hoekstra H., Yee H. K. C., Hall P. B., Barrientos L. F., 2003, ApJ, 593, 48
Gnedin O. Y., Kravtsov A. V., Klypin A. A., Nagai D., 2004, ApJ, 616, 16
Golse G., Kneib J.-P., 2002, A&A, 390, 821
Hattori M., Watanabe K., Yamashita K., 1997, A&A, 319, 764
Hennawi J. F. et al., 2008, AJ, 135, 664
Hilbert S., White S. D. M., Hartlap J., Schneider P., 2008, MNRAS, 386, 1845
Huterer D., Ma C.-P., 2004, ApJ, 600, L7
Johnson T. L., Sharon K., Bayliss M. B., Gladders M. D., Coe D., Ebeling H., 2014, ApJ, 797, 48
Jullo E., Natarajan P., Kneib J.-P., D'Aloisio A., Limousin M., Richard J., Schimd C., 2010, Science, 329, 924
Kaufmann R., Straumann N., 2000, Ann. Phys., 512, 384
Keeton C. R., 2001, ApJ, 562, 160
Kneib J.-P. et al., 2003, ApJ, 598, 804
Leauthaud A. et al., 2010, ApJ, 709, 97
Li G.-L., Mao S., Jing Y. P., Bartelmann M., Kang X., Meneghetti M., 2005, ApJ, 635, 795
Luppino G. A., Gioia I. M., Hammer F., Le Fèvre O., Annis J. A., 1999, A&AS, 136, 117
Meneghetti M., Bartelmann M., Moscardini L., 2003, MNRAS, 340, 105
Meneghetti M., Argazzi R., Pace F., Moscardini L., Dolag K., Bartelmann M., Li G., Oguri M., 2007, A&A, 461, 25
Meneghetti M. et al., 2014, ApJ, 797, 34
Merten J. et al., 2015, ApJ, 806, 4
Miralda-Escude J., Babul A., 1995, ApJ, 449, 18
Navarro J. F., Steinmetz M., 2000, ApJ, 538, 477
Navarro J. F., Frenk C. S., White S. D. M., 1996, ApJ, 462, 563

Newman A. B., Treu T., Ellis R. S., Sand D. J., Nipoti C., Richard J., Jullo E., 2013a, ApJ, 765, 24
Newman A. B., Treu T., Ellis R. S., Sand D. J., 2013b, ApJ, 765, 25
Oegerle W. R., Hill J. M., 2001, AJ, 122, 2858
Oguri M., Taruya A., Suto Y., 2001, ApJ, 559, 572
Oguri M., Lee J., Suto Y., 2003, ApJ, 599, 7
Oguri M., Takada M., Umetsu K., Broadhurst T., 2005, ApJ, 632, 841
Oguri M., Bayliss M. B., Dahle H., Sharon K., Gladders M. D., Natarajan P., Hennawi J. F., Koester B. P., 2012, MNRAS, 420, 3213
Pierre M., Soucail G., Boehringer H., Sauvageot J. L., 1994, A&A, 289, L37
Pimbblet K. A., Smail I., Edge A. C., O'Hely E., Couch W. J., Zabludoff A. I., 2006, MNRAS, 366, 645
Poggianti B. M., 1997, A&AS, 122, 399
Prada F., Klypin A. A., Cuesta A. J., Betancort-Rijo J. E., Primack J., 2012, MNRAS, 423, 3018
Rasia E., Borgani S., Ettori S., Mazzotta P., Meneghetti M., 2013, ApJ, 776, 39
Richard J. et al., 2010, MNRAS, 404, 325
Rozo E., Nagai D., Keeton C., Kravtsov A., 2008, ApJ, 687, 22
Sand D. J., Treu T., Ellis R. S., Smith G. P., 2005, ApJ, 627, 32
Schechter P., 1976, ApJ, 203, 297
Schindler S., 2000, A&AS, 142, 433
Schmidt R. W., Allen S. W., 2007, MNRAS, 379, 209
Schneider P., Ehlers J., Falco E. E., 1992, Gravitational Lenses. Springer-Verlag, Berlin
Struble M. F., Rood H. J., 1999, ApJS, 125, 35
Torri E., Meneghetti M., Bartelmann M., Moscardini L., Rasia E., Tormen G., 2004, MNRAS, 349, 476
Wambsganss J., Ostriker J. P., Bode P., 2008, ApJ, 676, 753
Wu X.-P., Hammer F., 1993, MNRAS, 262, 187
Xu B. et al., 2016, ApJ, 817, 85
Zaritsky D., Gonzalez A. H., Zabludoff A. I., 2006, ApJ, 638, 725

APPENDIX A: COMPARISON OF ARC STATISTICS OF RADIAL IMAGES VERSUS TANGENTIAL IMAGES

We proceed to obtain the number of arcs using equation (20) for radial images in axially symmetric profiles. In Fig. A1 left-hand panel we have reproduced (using different axis scaling) the lower-left panel of Fig. 1. In the right-hand panel of Fig. A1, we obtain the number of radial arcs for NFW profiles using the same combination of parameters that the left-hand panel. By comparing the left- and right-hand panel of Fig. A1, we find that tangential arcs are about one order of magnitude more numerous than radial arcs. Note that similar results are obtained if we compare the number of tangential and radial arcs for axially symmetric NSIS profiles (see Fig. A2).

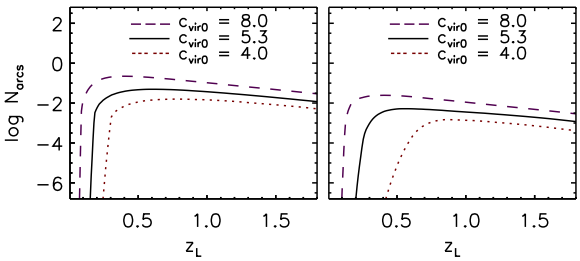

Figure A1. Tangential (left-hand panel) and radial (right-hand panel) number of arcs as a function of z_L in NFW profiles. The left-hand panel corresponds to the lower-left panel of Fig. 1 but with different scaling. The parameters to obtain the radial number of arcs in the right-hand panel are identical to those of the left-hand panel. Refer to legend in Fig. 1 for details in the selection of the lensing parameters.

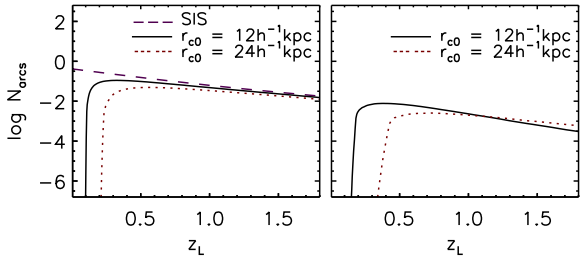

Figure A2. Tangential (left-hand panel) and radial (right-hand panel) number of arcs as a function of z_L in NSIS profiles. The left-hand panel corresponds to the left-hand panel of Fig. 2 but with different scaling. The parameters to obtain the radial number of arcs in the right-hand panel are identical to those of the left-hand panel. The absence of an SIS curve in the right-hand panel is due to the lack of radial images in this case. Refer to legend in Fig. 2 for details in the selection of the lensing parameters.

APPENDIX B: PSEUDO-ELLIPTICAL APPROXIMATION LIMITS OF VALIDITY

We test the validity of the pseudo-elliptical approximation by fitting an ellipse to the isodensity contours of κ_ϵ (obtained making $\kappa_\epsilon = \kappa_{\rm const}$ in equation 27a) at the intersection of the tangential critical curve with the x-axis ($x_t|_{\phi=0}$; x is the major axis). The fits were performed using the χ^2 minimization technique assuming the same error to a discretization of N angularly equidistant points ($\phi_{i+1} - \phi_i = \Delta\phi$). For this section, the fits were performed in one quadrant ($\phi_1 = 0$ and $\phi_N = \pi/2$) and a value of $N = 1000$ was used.

As in Dúmet-Montoya et al. (2012), we measure the goodness of the fit by quantifying the difference of the radial coordinate of the contour $r_\epsilon(\phi_i)$ and the radial coordinate of a fitted ellipse $r_\Sigma(\phi_i) = (a_\Sigma b_\Sigma)/\sqrt{(b_\Sigma \cos\phi)^2 + (a_\Sigma \sin\phi)^2}$ (with a_Σ and b_Σ semimajor and semiminor axis) from

$$\mathcal{D}^2 = \frac{\sum_{i=1}^{N} [r_\epsilon(\phi_i) - r_\Sigma(\phi_i)]^2}{\sum_{i=1}^{N} r_\epsilon(\phi_i)^2}. \quad \text{(B1)}$$

A value of $\mathcal{D}^2$ less than $\mathcal{D}^2_{\rm min} = 4.5 \times 10^{-4}$ indicates an acceptable minimum chi-squared fit ($\chi^2_\nu < \nu$; $\nu = N - 2$) with errors approximately equal to a factor $\mathcal{D}_{\rm min}$ of the squared root mean of the radial points.[9] We show comparisons of the pseudo-elliptical ellipticity ϵ with the fitted ellipticity $\epsilon_\Sigma = 1 - b_\Sigma/a_\Sigma$ for NFW models in Fig. B1 and NSIS models in Fig. B2. In Fig. B3, left-hand panel for NFW models and right-hand panel for NSIS models, we also show the maximum values ϵ ($\mathcal{D}^2 = \mathcal{D}^2_{\rm min}$) at which the pseudo-elliptical approximation remains valid. From Figs B1–B3, we find that for both the NFW and NSIS models the pseudo-elliptical approximation in general remains valid for $\epsilon \lesssim 0.3$ (or $\epsilon_\Sigma \lesssim 0.5$). However, for some extreme cases, like big values of $\kappa_s > 1.5$ in the NFW profile, or models with extreme low values of x_c in the NSIS profile, the pseudo-elliptical approximation breaks down at $\epsilon \sim 0.2$.

APPENDIX C: SURVEY OF ABELL CLUSTERS WITH STRONG LENSING

In our sample of Abell clusters, we looked for strong lensing by searching for tangentially elongated structures in the proximities

[9] Defining $\chi^2_\nu = (\nu\,\mathcal{D}^2)/\mathcal{D}^2_{\rm min} = \sum_{i=1}^{N} [r_\epsilon(\phi_i) - r_\Sigma(\phi_i)]^2/\sigma^2$ where $\nu = N - 2$. Under the assumption that the elliptical model is representative of the data and the errors $\sigma = \mathcal{D}_{\rm min}\sqrt{\sum_{i=1}^{N} r_\epsilon^2/\nu}$ are product of random fluctuations, we expect that χ^2_ν should follow a chi-squared distribution with ν degrees of freedom with mean equal to ν and variance equal to 2ν.

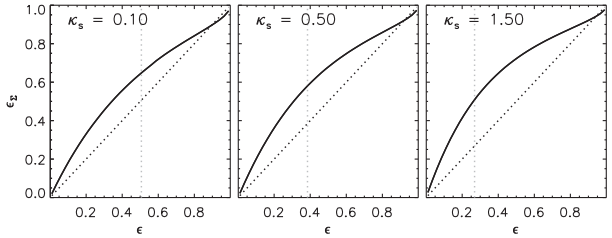

Figure B1. Fitted ellipticity (ϵ_Σ) of the pseudo-elliptical mass distribution as a function of ϵ. Each panel corresponds to NFW models with three different values of κ_s: in left-hand panel $\kappa_s = 0.1$, in central panel $\kappa_s = 0.5$ and in right-hand panel $\kappa_s = 1.5$. In each panel, the dotted diagonal line shows as reference $\epsilon_\Sigma = \epsilon$. Additionally, in each panel, the vertical dotted line indicates the maximum values of ϵ for which the pseudo-elliptical function is acceptable ($\mathcal{D}^2 = 4.5 \times 10^{-4}$, where $\mathcal{D}^2$ is given in equation B1).

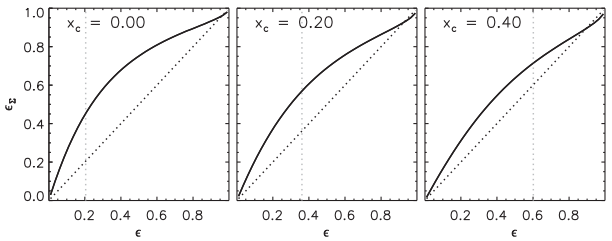

Figure B2. Fitted ellipticity (ϵ_Σ) of the pseudo-elliptical mass distribution as a function of ϵ. Each panel corresponds to NSIS models with three different values of x_c: in left-hand panel $x_c = 0.0$ (SIS), in central panel $x_c = 0.2$ and in right-hand panel and $x_c = 0.4$. For reference about dotted lines see legend of Fig. B1.

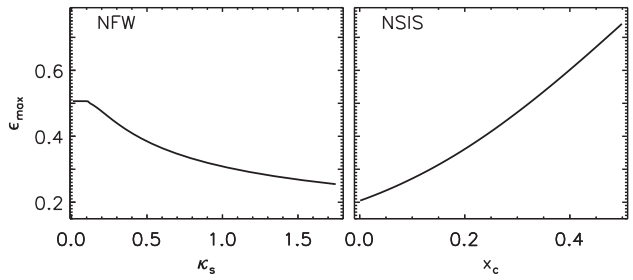

Figure B3. Maximum value of the ellipticity for which the pseudo-elliptical approximation is acceptable ($\mathcal{D}^2 = 4.5 \times 10^{-4}$, where $\mathcal{D}^2$ is given in equation B1). Left-hand panel: NFW model, x-axis is κ_s. Right-hand panel: NSIS model, x-axis is x_c.

(within 1 arcmin) of the BCG. We found evidence of these structures in eight (out of 49) clusters, A0907, A1084, A1451, A2029, A2104, A2163, A2204 and A2744 (see Fig. C1). In the rest of this section, we provide a brief description of the lensing structures (see Fig. C1) and references for cases (five out of eight) where strong lensing have been already found in the literature.

Figure C1. Strong lensing candidates in out X-ray bright Abell cluster sample. Each panel is a 60 arcsec × 60 arcsec region around the BCG; north is up and east to the left. The panels starting from top-left clockwise are: A0907, A1084, A1451, A2029, A2104, A2163, A2204 and A2744.

A0907. There is one elongated arc in the north-west side of the BCG.

A1084. Evidence of strong lensing was previously noticed in Sand et al. (2005). As shown in Fig. C1, there are two arc-like structures that are tracing a circular region around the BCG of ≈19 arcsec of radius. The brightest arc-like structure is at the southern side of the BCG, the other arc-like structure is at the northwestern side of the BGC. Given the distribution of the structures it is very likely that these are images of the same galaxy.

A1451. There is one significantly bright arc with length ≈10 arcsec at the northern side of the BCG.

A2029. There is one ≈16 arcsec elongated arc it the southern tip of the BCG that looks very faint in Fig. C1 due to saturation of light from the central galaxy. This is the lowest redshift cluster in our sample ($z = 0.077$) with evidence of strong lensing.

A2104. There is one bright ≈12 arcsec arc it the northeastern tip of the BCG as already noticed by Pierre et al. (1994).

A2163. As noticed by Miralda-Escude & Babul (1995), there are two tangentially elongated galaxies in the southwestern side of the BCG. These two red colour galaxies in Fig. C1 form an arc-like structure of ≈18 arcsec.

A2204. Evidence of strong lensing was previously noticed in Sand et al. (2005) and Richard et al. (2010). As shown in Fig. C1, there are several conspicuous arclets forming a circular structure around the central BGG. The most prominent strong lensing feature is an ≈15 arcsec arc at the south of the BCG.

A2744. Evidence of arcs and detailed strong lensing models of this cluster are presented in Sand et al. (2005) and Johnson et al. (2014), respectively. In our observations, as shown in Fig. C1 the most clear arc candidate shows in blue colour at the southwestern side of the BCG. Note that surrounding the BCG there other two smaller blue arclets as well.

This paper has been typeset from a TEX/LATEX file prepared by the author.